Dynamics of photoexcited Ba$^+$ cations in ^{4}He nanodroplets

Antonio Leal,[1] Xiaohang Zhang,[2] Manuel Barranco,[1,3] Fausto Cargnoni,[4]
Alberto Hernando,[5] David Mateo,[6] Massimo Mella,[7] Marcel Drabbels,[2] and Martí Pi[1]

[1]*Departament ECM, Facultat de Física, and IN^{2}UB, Universitat de Barcelona, Diagonal 645,
08028 Barcelona, Spain*
[2]*Laboratoire de Chimie Physique Moléculaire, Swiss Federal Institute of Technology Lausanne (EPFL),
CH-1015 Lausanne, Switzerland*
[3]*Laboratoire des Collisions, Agrégats, Réactivité, IRSAMC, UMR 5589, CNRS et Université
Paul Sabatier-Toulouse 3, 118 route de Narbonne, F-31062 Toulouse Cedex 09, France*
[4]*Istituto di Scienze e Tecnologie Molecolari (ISTM), Consiglio Nazionale delle Ricerche, via Golgi 19,
20133 Milano, Italy*
[5]*Social Thermodynamics Applied Research (SThAR), EPFL Innovation Park, Bâtiment C,
CH-1015 Lausanne, Switzerland*
[6]*Department of Chemistry and Biochemistry, California State University at Northridge, Northridge,
California 91330, USA*
[7]*Dipartimento di Scienza ed Alta Tecnologia, Università degli Studi dell'Insubria, via Valleggio 11,
22100 Como, Italy*

We present a joint experimental and theoretical study on the desolvation of Ba$^+$ cations in ^{4}He nanodroplets excited via the 6p ← 6s transition. The experiments reveal an efficient desolvation process yielding mainly bare Ba$^+$ cations and Ba$^+$He$_n$ exciplexes with $n = 1$ and 2. The speed distributions of the ions are well described by Maxwell-Boltzmann distributions with temperatures ranging from 60 to 178 K depending on the excitation frequency and Ba$^+$ He$_n$ exciplex size. These results have been analyzed by calculations based on a time-dependent density functional description for the helium droplet combined with classical dynamics for the Ba$^+$. In agreement with experiment, the calculations reveal the dynamical formation of exciplexes following excitation of the Ba$^+$ cation. In contrast to experimental observation, the calculations do not reveal desolvation of excited Ba$^+$ cations or exciplexes, even when relaxation pathways to lower lying states are included. © *2016 AIP Publishing LLC*. [http://dx.doi.org/10.1063/1.4942850]

I. INTRODUCTION

Ever since the first ion drift experiments in liquid helium by Williams in 1957,[1] ions have played a crucial role in elucidating the properties of superfluid ^{4}He. One of the highlights is undoubtedly the experimental determination of the critical Landau velocity.[2] The helium solvation structure surrounding ions depends strongly on their charge. Due to the Pauli repulsion an electron is located in a region void of helium with a radius of typically 17 Å,[3,4] giving this structure a large effective hydrodynamic mass.[5] The structure around positive ions is very different as electrostriction leads to the formation of high density helium shells ("snowballs") around cations.[6,7] Details about these solvation structures can be inferred from ion mobility experiments.[8] In this context, alkali earth cations are of special interest since their structure is determined by the balance between electrostriction due to the charge and the Pauli repulsion experienced by the unpaired electron. Additional insight in the solvation structure can be obtained from the spectroscopic investigation of the solvated species, as spectra are strongly affected by the interaction of the solute with helium. While most experiments have focussed on the neutral species,[9] also spectra of cations have been recorded, most notably Ba$^+$.[10] The excitation spectrum corresponding to the 6p ← 6s transition of Ba$^+$ is found to

be substantially broadened and blue-shifted with respect to the gas phase. In agreement with the ion mobility solvation structure determination, the characteristics of the spectrum could be largely reproduced by a bubble model.[11]

Compared to bulk helium, the solvation of atoms and molecules is much less challenging when using helium nanodroplets.[12] As a result, most spectroscopic studies on solutes in helium are performed using helium droplets, see, for example, Refs. 13–15. From these experiments, the temperature of the ^{4}He droplets could be established to be 0.38 K.[16] The electronic and vibrational spectra of glyoxal and OCS, respectively, provided strong indications that these finite size helium droplets are superfluid at this temperature.[17,18] Recent drift experiments in helium droplets where neutral atoms and molecules have been accelerated out of droplets by electronic excitation have revealed the existence of a critical Landau velocity in these droplets.[19]

In contrast to the large body of literature on the spectroscopy of neutral species in helium droplets, that involving ions is rather limited due to the technical challenges associated with the production of ion containing droplets.[20–22] Initial spectroscopic studies on ions in helium droplets have revealed that the effect of the helium on the spectra of charged species is similar as for neutral species. Similar to neutrals, electronic spectra are characterized by sharp

zero-phonon lines and broad phonon wings,[23] while vibrational spectra are characterized by narrow transitions and small helium induced matrix shifts.[24–26] Whereas the spectroscopy for neutral and charged species is very similar, their dynamics appear to be different. Vibrational excitation of a neutral is followed by a fast transfer of the photon energy from the molecule to the helium leading to the shrinking of the helium droplet by evaporation of atoms from its surface.[27] In contrast, vibrational excitation of ions in helium droplets is found to lead to a nonthermal desolvation process in which the ions are ejected from the droplets.[24,28,29] To disentangle the role of vibrational and electronic excitation, the desolvation of excited of Ba^+ cations embedded in helium droplets has recently been investigated.[30] Here, in an attempt to elucidate the desolvation process of ions, we report more elaborate experiments on this system accompanied with a theoretical modeling of the dynamics. The calculations are based on a time-dependent density functional description of the helium combined with classical dynamics for the excited Ba^+ cation. Helium density functional calculations have been very successful in the past in describing static properties of doped helium droplets, see, e.g., Ref. 31 and references therein. Recently the time-dependent version has been successfully applied to describe various dynamical processes, like the capture of atoms by helium droplets,[32] the solvation of ions,[33,34] and the desorption of atoms from helium droplets.[35–37] Here we apply this method to investigate the dynamics of excited Ba^+ ions in helium nanodroplets.

II. EXPERIMENTAL

A. Setup

Details of the experiment and the experimental setup have been reported before.[30,38,39] Helium droplets are formed by expanding He gas at stagnation pressure of 30 bars into vacuum through a cryogenically cooled 5 μm orifice. The size distribution of these droplets can be systematically varied by changing the source temperature.[40] The helium droplets on average pick up less than one Ba atom as they pass through a heated oven containing barium dendritic crust. Via a differential pumping stage the doped droplets enter a velocity map imaging setup where the droplet beam is crossed at right angles by two counter-propagating laser beams. The barium-doped helium droplets are ionized by one-photon absorption of a 42 283 cm^{-1} photon from a frequency-doubled Nd:YAG pumped dye laser. After a time delay of 185 ns, the barium ions are excited via the 6p ← 6s transition by visible radiation in the wavelength range of 430-500 nm provided by another Nd:YAG pumped dye laser. The ions are accelerated towards a position sensitive detector consisting of a set of microchannel plates and a phosphor screen. A high-resolution CCD camera takes snapshots of the phosphor screen at each laser shot. The individual images are analyzed online and the centroids of the ion impacts are determined. The velocity distributions of the ions are determined by performing an inverse Abel transform on the images constructed from the accumulated centroids. Ion images can be recorded at a specific mass or masses by gating the front of the detector at the arrival time of the ions

of interest. By feeding the electrical signal from the phosphor screen into a multichannel scaler, time-of-flight mass spectra can be recorded.

B. Results

As previously reported, upon ionization of the Ba atoms the created Ba^+ ions become solvated by the helium on a picosecond time scale.[30,34] Excitation of the solvated ions via the 6p ← 6s transitions subsequently leads their desolvation. The corresponding spectrum, recorded by monitoring the yield of desolvated ions as a function of excitation frequency can be found in Fig. 1 of Ref. 30. The D1 and D2 lines, corresponding to the $^2P_{1/2} ← {}^2S_{1/2}$ and $^2P_{3/2} ← {}^2S_{1/2}$ transition, respectively, are broadened and blue-shifted by approximately 500 cm^{-1} compared to the gas phase. The D2 line shows an additional splitting of ∼400 cm^{-1}. The product distribution of the desolvated ions has been determined by time-of-flight mass spectrometry at three excitation frequencies, 20 714, 22 425, and 22 845 cm^{-1}, corresponding to the D1 and the two D2 absorption maxima, respectively. Analysis of the mass spectra reveals that approximately half of all ions are fully desolvated, while the other half carries along one or more helium atoms, see Fig. 1 which reports the relative Ba^+He_n product yield. The Ba^+He_n product distributions depend weakly on the spin-orbit state and are found to extend up to $n = 25$. Excitation via the D1 transition yields the smallest amount of bare Ba^+ ions and a nearly similar amount of Ba^+He. Excitation of the D2 transition at low frequency yields the maximum amount of bare Ba^+ ions. Interestingly, excitation at the high frequency part of the D2 transitions yields a slightly different product distribution with a relatively large amount of Ba^+He_n exciplexes with $4 ≤ n ≤ 8$.

In order to gain insight into the desolvation mechanism of the excited ions their speed distributions have been determined by velocity map imaging. A typical image is shown in the inset of Fig. 2. It has been recorded following excitation via the D1 transition of Ba^+ ions solvated in droplets consisting on average of 4000 helium atoms before pickup of Ba. The image is characterized by an isotropic angular and a smooth radial distribution. The speed distribution derived
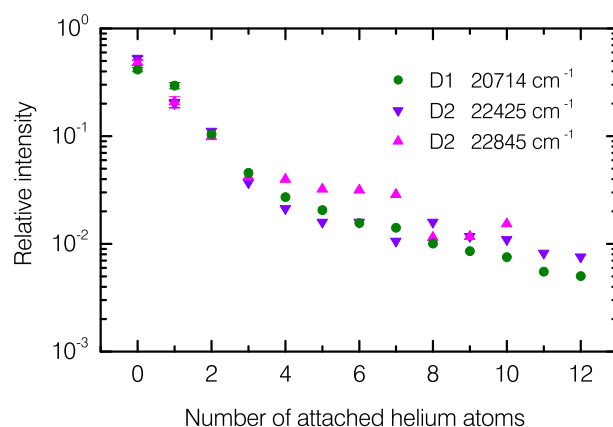

FIG. 1. Relative yield of Ba^+He_n exciplexes at selected excitation frequencies determined from time-of-flight mass spectra recorded for Ba^+ in droplets containing an average of 4000 helium atoms before pickup of Ba.

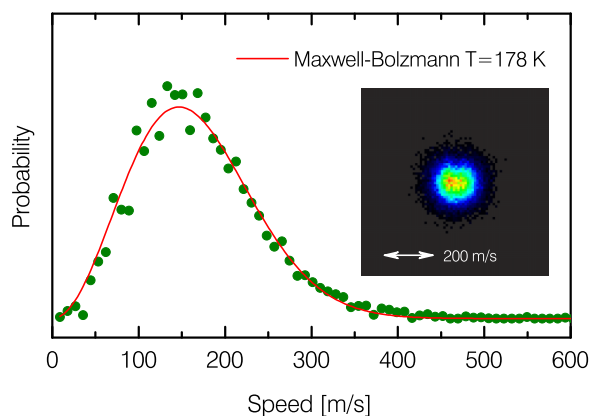FIG. 2. Velocity map image (inset) and derived speed distribution recorded following excitation via the D1 transition at 20 714 cm^{-1} of Ba$^+$ embedded in droplets containing on average 4000 helium atoms. The solid line is a fit to a Maxwell-Boltzmann distribution corresponding to a translational temperature of 178 K.

from this image is shown in Fig. 2 and follows a Maxwell-Boltzmann distribution. A fit of the data yields a translational temperature for these ions of 178 ± 4 K. The resulting temperature is found to be independent of the size of the droplets and laser intensity. Excitation via the D2 transition yields also an isotropic angular and a Maxwell-Boltzmann speed distribution. Although the photon energy in this case is larger, the translational temperature is significantly lower, i.e., 96 ± 4 K. This temperature is found to be independent of droplet size, laser intensity, and excitation frequency within the D2 band. In addition to the velocity distributions of bare Ba$^+$ ions, those of the Ba$^+$He$_n$ exciplexes have been determined. These too can be accurately described by Maxwell-Boltzmann distributions. The resulting translational temperatures are presented in Fig. 3. For excitation via the D1 transition one observes a rapid decay of the translational temperature with increasing number of helium atoms. For the larger exciplexes the temperature gradually levels off to a value of ∼60 K. Excitation via the D2 transitions yields a clearly different temperature variation with the number of helium atoms. After a decay of the translational temperature for Ba$^+$He, it increases again for larger exciplexes before leveling
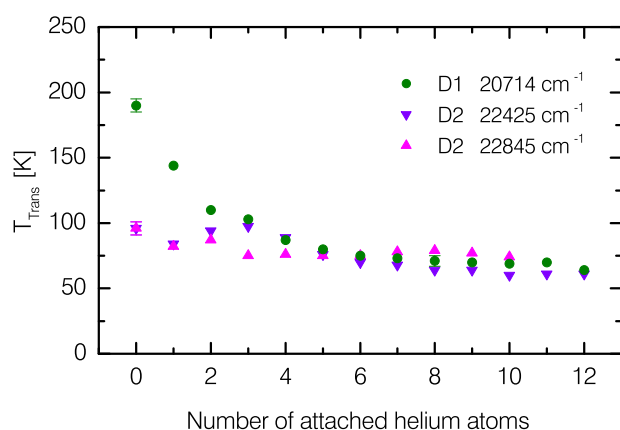

FIG. 3. Translational temperature of desolvated Ba$^+$ and Ba$^+$He$_n$ exciplexes determined from speed distributions recorded following excitation of Ba$^+$ at selected frequencies.

off at approximately 60 K for the largest exciplexes. The temperatures of all species are significantly larger than the effective temperature corresponding to Ba$^+$ moving with the critical Landau velocity of 58 m/s, i.e., 28 K, indicating that the desolvation mechanism differs from that of Ag.[19]

The difference between the Ba$^+$He$_n$ exciplex distributions and the translational temperatures of the exciplexes for D1 and D2 excitation clearly indicates that the dynamics induced by the excitation of the ions depends on the excited state. Spectroscopic studies of Ba$^+$ in bulk have revealed that 6p ^{2}P$_{3/2}$ population relaxes quickly to the 6p ^{2}P$_{1/2}$ state.[10] Consequently, one has to conclude that the overall dynamics is significantly affected by the 6p ^{2}P$_{3/2}$ → 6p ^{2}P$_{1/2}$ relaxation process. Unfortunately, it is not possible to deduce any further details on the dynamics from the experimental data. To gain insight we have therefore performed dynamical simulations of excited Ba$^+$@He$_{1000}$ where we combine a classical treatment of the Ba$^+$ ion with a time-dependent DFT (TDDFT) description of the helium.

III. THEORETICAL APPROACH

A. He–Ba$^+$ pair potentials

One of the key ingredients for the dynamical simulations presented in this study are the potential energy curves (PECs) of the ground ^{2}S and the excited ^{2}P and ^{2}D states of the Ba$^+$–He dimer. Accurate PECs for this system have recently been computed by some of the present authors.[34,41] This section describes their salient features as well as additional calculations providing further support to their accuracy.

The available ground state potential[34] has been determined at the CCSD(T) level of theory using a high quality basis set both for Ba$^+$ and He, plus a set of bond functions placed midway between the two nuclei. As a test of the reliability of this PEC, we have conducted additional computations using the same level of theory, basis set for He, and set of bond functions, but a different pseudopotential for the core electrons of Ba$^+$ (Ref. 42) and a larger basis set for its valence electrons (QZVP).[43] The latter consists of 7s6p4d2f1g gaussian functions instead of 7s5p3d1f. The position of the minimum interaction energy and of the PEC turning point (i.e., the internuclear distance where the interaction potential becomes repulsive) shift towards shorter distances by less than 0.05 Å, and the attractive well becomes more attractive by roughly 2%. Such variations are not expected to play any relevant role in the dynamics of Ba$^+$–He$_N$ aggregates when Ba$^+$ is in the electronic ground state, and hence in this study we adopted the interatomic potential presented in Ref. 34.

The Ba$^+$–He excited states relevant to the present investigation (the lowest ^{2}D and ^{2}P states) have already been determined using two variational approaches, i.e., Configurations Interaction including single and double excitations (CISD), and Multi-Reference Configurations Interaction (MRCI) containing up to triple excitations.[41] The two sets of potentials are quantitatively very similar, suggesting that the interaction energy is determined essentially by the induction component, the electron dispersion energy, and the Pauli repulsion at short internuclear distances.

Indeed, these terms are well described by single and double excitations, with minor contributions coming from higher order excitations, as already observed in the interaction between neutral coinage metal atoms and He.[44] As a possible alternative, we have tested a perturbative approach at second order, Multi-Configuration Quasi-Degenerate Perturbation Theory (MCQDPT) as implemented in the GAMESS-US computational code,[45] adopting the same pseudopotential and basis sets of the MRCI potentials.[41]

The ^2P excited state splits into a $^2\Sigma$ and two degenerate $^2\Pi$ states in Ba$^+$–He (spin-orbit effects are not considered at this stage). The $^2\Sigma$ state is highly repulsive, as the Ba$^+$ outermost electron occupies a p orbital pointing towards the helium atom. CISD, MRCI, and MCQDPT computations for this state yield very similar results, with differences in interaction energy measuring just a few percent along the entire range of internuclear distances considered. The PEC of the $^2\Pi$ state exhibits an attractive well due to the Ba$^+$ outermost electron occupying a p orbital perpendicular to the Ba$^+$–He internuclear axis, which allows the He to interact with the unscreened Ba$^+$ core. The attractive well predicted by the perturbative computations (516 cm^{-1} at the MCQDPT level) is more attractive by about 6% compared to variational data (485 cm^{-1} at the MRCI level of theory), and the turning point of the potential is shifted by few hundredths of an Å towards shorter distances.

The lower lying ^2D state splits into a single $^2\Sigma$ and two sets of doubly degenerate $^2\Pi$ and $^2\Delta$ states. The $^2\Sigma$ is highly repulsive, as the outermost electron of Ba$^+$ occupies the d orbital directed towards the He atom. We found no relevant differences among the CISD, MRCI, and MCQDPT potentials. The $^2\Pi$ and $^2\Delta$ states have quite large well depths of 373 cm^{-1} and 220 cm^{-1}, respectively, at the MRCI level. Perturbative computations predict the attractive well to be deeper by about 15% compared to the MRCI data, and the PEC to shift to shorter distances by about 0.10 Å.

Analogously to the ground state, the differences among the available potentials and the MCQDPT data are not expected to play a relevant role in the simulations of the dynamics of Ba$^+$–He$_N$ aggregates following excitation. In the present investigation we adopt the MRCI potentials[41] for the description of ^2P and ^2D states. To aid the discussion of the results, we present in Fig. 4 the PEC corresponding to the ^2S, ^2P, and ^2D states with the spin-orbit interaction included as discussed in Refs. 41 and 46. The ^2S ground state PEC has already been used in the past to address the solvation of Ba$^+$ in helium nanodroplets.[33,34]

B. Static density functional theory (DFT)

Before starting dynamical calculations we first consider the energetics of the system using static DFT calculations. Barium atoms captured by helium droplets are known to reside in a dimple at the surface of the droplet,[47,48] an experimental fact well reproduced by DFT calculations.[49] If the Ba atom is subsequently photoionized, the resulting cation becomes solvated by the helium by sinking into the droplet.[30,34]

The energy available for this process is determined by the energy difference between the equilibrium configuration,
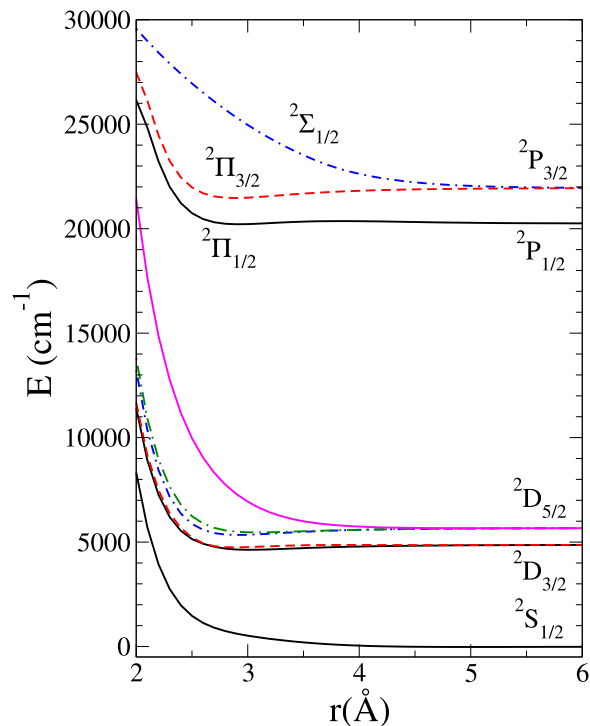

FIG. 4. ^2S, ^2P, and ^2D Ba$^+$–He pair potentials. The splitting introduced by the spin-orbit interaction has been included.

corresponding to Ba$^+$ at the center of the droplet, and that corresponding to Ba$^+$ residing at the surface dimple. Both of these can be obtained by static DFT calculations. We have considered a droplet made of $N = 1000$ helium atoms and have first obtained the structure of the neutral Ba-droplet complex in the ground state. In view of the large mass of barium compared to that of helium, we describe the Ba atom and its cation as classical particles in the dynamics while their effect on the statics is incorporated as an external field acting upon the droplet.[36,50] Accordingly, the energy of the system is written as

$$E[\rho] = \int d\mathbf{r} \left\{ \frac{\hbar^2}{2m_{He}} |\nabla\sqrt{\rho(\mathbf{r})}|^2 + \mathcal{E}_{He}[\rho(\mathbf{r})] \right\}$$
$$+ \int d\mathbf{r}\, \rho(\mathbf{r})\, V_X(|\mathbf{r}_{Ba} - \mathbf{r}|), \tag{1}$$

where $\mathcal{E}_{He}$ is the potential energy density per unit volume, $\rho(\mathbf{r})$ is the He atom density at point $\mathbf{r}$, and $\mathbf{r}_{Ba}$ is the impurity location.

The Ba$^+$–He and Ba–He ground state pair potentials V_X have been taken from Refs. 34 and 51, respectively. The density functional (DF) used in the present work is a modified version of the Orsay-Trento functional[52] able to handle very structured helium configurations as those expected to appear around fairly attractive impurities such as cations.[53]

Upon variation of Eq. (1) one obtains the Euler-Lagrange equation. The equilibrium helium density $\rho_0(\mathbf{r})$ and the location of the dopant atom $\mathbf{r}_{Ba_0}$ can be determined from

$$\left\{ -\frac{\hbar^2}{2m_{He}} \nabla^2 + \frac{\delta}{\delta\rho} \mathcal{E}_{He} + V_X(|\mathbf{r}_{Ba} - \mathbf{r}|) \right\} \Psi_0(\mathbf{r}) = \mu\, \Psi_0(\mathbf{r}), \tag{2}$$

where μ is the chemical potential of the He droplet and $\Psi_0(\mathbf{r}) \equiv \sqrt{\rho_0(\mathbf{r})}$. Eq. (2) has been solved in Cartesian coordinates using a spatial grid of 0.4 Å. The derivatives have been calculated with 13-point formulas. Extensive use of fast-Fourier techniques[54] has been made to efficiently calculate the energy density and mean field potential.

A two-dimensional view of the dimple state configuration of the neutral Ba atom can be seen in Fig. 2 of Ref. 34. The Ba atom is located 22.6 Å away from the center of the $^4\text{He}_{1000}$ droplet. Upon photoionization, the energy of the cation sitting at this position is obtained from Eq. (1) using the non-relaxed helium density and the Ba^+–He ground state pair potential. This yields an energy of -5622 K for the $\text{Ba}^+@^4\text{He}_{1000}$ system (the DFT energy of the pure $^4\text{He}_{1000}$ droplet is -5401 K). The helium density profile of $\text{Ba}^+@^4\text{He}_{1000}$ corresponding to the equilibrium position at the center of the droplet can be seen in Fig. 3 of Ref. 33. It has an energy of -6461 K. If we assume that the outgoing electron created in the ionization process does not transfer energy to the helium, an assumption justified by the corresponding photoelectron spectrum,[48] the energy deposited into the droplet by the photoionization process is calculated to be 839 K. In the course of the dynamics, part of this energy will be taken away by ejected helium atoms[34] and part will remain in the system shared between kinetic energy of the impurity and excited droplet modes.

Quasi-static Ba^+-droplet configurations in which the cation resides at a fixed distance from the center-of-mass (COM) of the helium moiety can be obtained by a constrained energy minimization.[55] Fig. 5 shows the energy of these quasi-static configurations, which we will refer to as "stretched configurations," as a function of the distance between the cation and the center-of-mass of the helium moiety, $\mathcal{Z}_0$. The energies are referenced to the equilibrium energy corresponding to $\mathcal{Z}_0 = 0$. The distance corresponding to the equilibrium position of the neutral Ba atom is indicated by an arrow. At this distance the energy of the stretched configuration is smaller than the energy deposited into the droplet upon ionization of the neutral Ba. This difference is because the stretched helium configuration has been obtained by minimization of the constrained energy whereas this is not the case for the dimple configuration, as discussed above.

If the system is stretched far enough, the droplet-Ba^+ complex breaks into a "charged minicluster" containing some 170 helium atoms tightly bound to the Ba^+ cation plus a neutral droplet with the remaining helium. Fig. 5 shows that the charged minicluster configuration is energetically favorable for $\mathcal{Z}_0 \gtrsim 38$ Å. Before the breaking, the stretched configurations display a preformed charged minicluster connected to the rest of the droplet by a "neck." Fig. 5 also shows the existence of metastable configurations of either kind before and after the crossing point. Also shown are the densities of a stretched and a minicluster configuration corresponding to $\mathcal{Z}_0 = 37.6$ Å whose energies only differ by 6.5 K. It is worth nothing that the system has to be significantly stretched to reach the scission point where the charged minicluster configuration appears, i.e., some 15 Å away from the original location of the neutral Ba atom on the droplet surface, whose radius is 22.2 Å for $N = 1000$. Such stretched
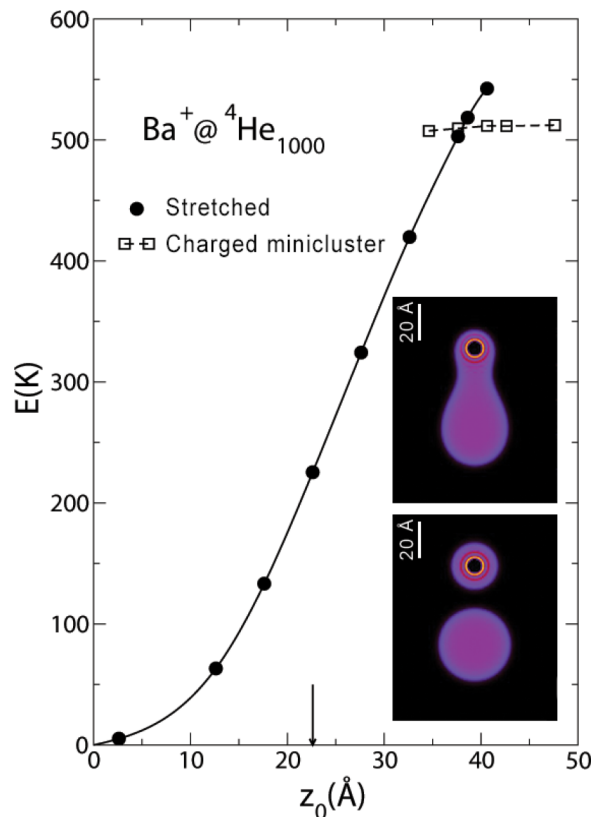

FIG. 5. Energy of the stretched configuration (solid line) as a function of the distance to the COM of the helium moiety. The dashed line represents the energy of the charged minicluster configuration. Both energies are referred to that of the equilibrium configuration of Ba^+ at the center of the droplet (-6461 K). Indicated by an arrow is the distance of the neutral Ba at the dimple surface to the center of the helium droplet before photoionization. Also shown are stretched and charged minicluster configurations, the latter containing about 170 He atoms, corresponding to $\mathcal{Z}_0 = 37.6$ Å.

scission configurations have been found in the past for the fission of ^3He droplets.[56]

This analysis indicates that the energy deposited into the droplet by the photoionization of the neutral Ba at the dimple (839 K) is in principle large enough to allow the appearance of stretched configurations leading to charged minicluster formation (509.5 K). However, actual dynamic calculations[36] indicate that this is rather unrealistic. We therefore conclude that the desolvation of excited Ba^+ cations as observed experimentally is not related to charged miniclusters formed upon ionization of the system.

To address the dynamics of the excited Ba^+ ion one has to resort to a time-dependent description. The more ambitious strategy consists of modeling the experiment, starting from the photoionization of the neutral Ba atom at the surface dimple and followed by the photoexcitation of the Ba^+ cation some time after its creation. The first part of this process has been reported in Ref. 34 where the dynamics of the cation in the ground state was followed for more than 200 ps. This is a long time period for the calculations but short compared to the experimental time scale. In the experiments the time delay between ionization and excitation is 185 ns using laser pulses having a duration of 5 ns. A less ambitious strategy assumes that during its dynamic evolution the ground state

Ba$^+$ cation has been taken to a stretched configuration from which it is then photoexcited to the ^{2}P manifold. In either approach, one might expect that excitation can lead to the desolvation of the cation either because the interaction of the droplet with the excited cation is repulsive—as in the case for the silver atom[36]—or because the helium supersonic density waves launched in the excitation process break the "neck" of the stretched configuration and simultaneously remove a sizable number of helium atoms initially located around the excited cation.

C. Time-dependent DFT

The dynamics presented in this work haven been obtained within the TDDFT approach.[57,58] We refer the reader to Refs. 32–37 for a thorough discussion of the approach and how it has been implemented in some applications. For the sake of completeness and to aid the discussion, we briefly discuss the method of Ref. 36. The basic ingredients are the Born-Oppenheimer approximation that allows to factorize the electronic and nuclear wave functions, the Franck-Condon approximation which assumes that the atomic nuclei do not change their positions or momenta during the electronic transition,[59] and the use of the diatomics-in-molecule approximation[60] that combined with DFT to describe the droplet-impurity complex allows factorizing the impurity and He nuclear components.

We introduce a complex effective wave function $\Psi_{He}(\mathbf{r},t)$ representing the helium moiety that is evolved following the TDDFT prescription. The displacement of the cation position $\mathbf{r}_{Ba^+}(t)$ is treated classically. The spin-orbit (SO) interaction is included as indicated in Ref. 61, by writing the electron angular momentum in Cartesian coordinates $i = x, y, z$ and the spin state as $s = \uparrow (m_s = 1/2), \downarrow (m_s = -1/2)$. The magnitude of the SO interaction is fixed to reproduce the spin-orbit splitting of bare Ba$^+$ in the 6p ^{2}P states being 1690.84 cm^{-1}.[62]

The evolution of the electronic excited state of Ba$^+$ is described by introducing an additional degree of freedom, a six-component vector $|\lambda\rangle$ written in terms of same basis for spin and angular momentum used for the SO interaction

$$|\lambda\rangle = \sum_{is} \lambda_{is}|i,s\rangle. \qquad (3)$$

The vector is normalized $|\langle\lambda|\lambda\rangle|^2 = 1$. Notice that states as, e.g., $|x\uparrow\rangle$ are referred to in the literature as $p_x \uparrow$.[59] The complete set of dynamical variables characterizing the system thus consists of a complex effective wavefunction for helium $\Psi_{He}(\mathbf{r},t)$ such that $\rho(\mathbf{r},t) = |\Psi_{He}(\mathbf{r},t)|^2$, a vector position for the impurity, $\mathbf{r}_{Ba^+}(t)$, and a 6-dimensional complex vector for its electronic state $|\lambda(t)\rangle$. The total energy of the Ba$^+$@^{4}He$_{1000}$ complex suddenly excited to the ^{2}P manifold is written as

$$E[\Psi, \mathbf{r}_{Ba^+}, \lambda] = \int d\mathbf{r} \frac{\hbar^2}{2m_{He}}|\nabla\Psi|^2 + \frac{p_{Ba^+}^2}{2m_{Ba^+}}$$
$$+ \int d\mathbf{r} \, \mathcal{E}_{He}[\rho] + \langle\lambda|V_{SO}|\lambda\rangle$$
$$+ \int d\mathbf{r} \, \rho(\mathbf{r}) \, V_\lambda(\mathbf{r} - \mathbf{r}_{Ba^+}). \qquad (4)$$

We have followed the prescription of Ref. 61 to write the pair potential as a direction-dependent combination of Π and Σ potentials determined in Ref. 41,

$$V_\lambda(\mathbf{r}) = \langle\lambda|\mathcal{V}(\mathbf{r})|\lambda\rangle = \sum_{ijss'} \lambda_{is}^* \mathcal{V}^{ijss'}(\mathbf{r})\lambda_{js'}, \qquad (5)$$

where the six-dimensional matrix operator $\mathcal{V}$ has components

$$\mathcal{V}^{ijss'}(\mathbf{r}) = \left[V_\Pi(r)\delta_{ij} + (V_\Sigma(r) - V_\Pi(r))\frac{r_i r_j}{r^2}\right]\delta_{ss'}. \qquad (6)$$

The following coupled 3D time-dependent system, resulting from the variation of the action, has to be solved to obtain the dynamical evolution of the system

$$i\hbar\frac{\partial}{\partial t}\Psi_{He} = \left[-\frac{\hbar^2}{2m_{He}}\nabla^2 + \frac{\delta\mathcal{E}_{He}}{\delta\rho(\mathbf{r})} + V_\lambda(\mathbf{r} - \mathbf{r}_{Ba^+})\right]\Psi_{He}$$

$$i\hbar\frac{\partial}{\partial t}|\lambda\rangle = \mathcal{H}\,|\lambda\rangle,$$

$$m_{Ba^+}\ddot{\mathbf{r}}_{Ba^+} = -\nabla_{\mathbf{r}_{Ba^+}}\left[\int d\mathbf{r}\rho(\mathbf{r})V_\lambda(\mathbf{r} - \mathbf{r}_{Ba^+})\right] \qquad (7)$$

$$= -\int d\mathbf{r}\,\nabla\rho(\mathbf{r})V_\lambda(\mathbf{r} - \mathbf{r}_{Ba^+}),$$

where the t-dependence of the dynamical variables is omitted for clarity. The electronic state Hamiltonian $\mathcal{H}$ is a 6×6 matrix whose elements are given by

$$H^{ijss'} = \int d\mathbf{r}\,\rho(\mathbf{r})\mathcal{V}^{ijss'}(\mathbf{r} - \mathbf{r}_{Ba_0^+}) + V_{SO}^{ijss'}. \qquad (8)$$

Equations (7) have been solved within the same box and using the same grid as for the static problem. The time step employed is 0.5 fs. We have used a predictor-modified-corrector method[63] fed by a few time steps obtained by a fourth-order Runge-Kutta-Gill algorithm.[63] When the energy deposited into the helium droplet is high enough as a consequence of the occurring physical process, it may happen that some helium density, representing evaporated helium atoms, leaves the droplet and eventually hits the box boundary. To prevent that these usually few "atoms" bounce back, we have included an absorbing potential.[64] As a result, particle—and thus energy—leaking appears when some helium density arrives near the walls of the calculation box where the absorbing potential acts. This leaking represents helium atoms leaving the droplet and the energy carried away by them.

To solve Eqs. (5)–(8) initial values for the variables are required. As starting configuration we have chosen that corresponding to the turning point reached by the Ba$^+$ in the ground state 223 ps after the ionization of neutral Ba in the surface dimple state.[34] At this time, the distance between the cation and the COM of the droplet is 11.1 Å. The associated helium density $\rho_0(\mathbf{r})$—or effective wave function $\Psi_0(\mathbf{r})$—and cation position $\mathbf{r}_{Ba_0^+}$ define the initial conditions, as $\dot{\mathbf{r}}_{Ba_0^+} = 0$ at the turning point. This starting configuration is shown in the top left panel of Fig. 6, together with the corresponding V_λ potentials.

There remains to fix the initial $|\lambda\rangle$ state. This has been done by choosing one of the eigenstates resulting from the diagonalization of the Hamiltonian $\mathcal{H}$ at the time of excitation. If the helium density is spherically symmetric
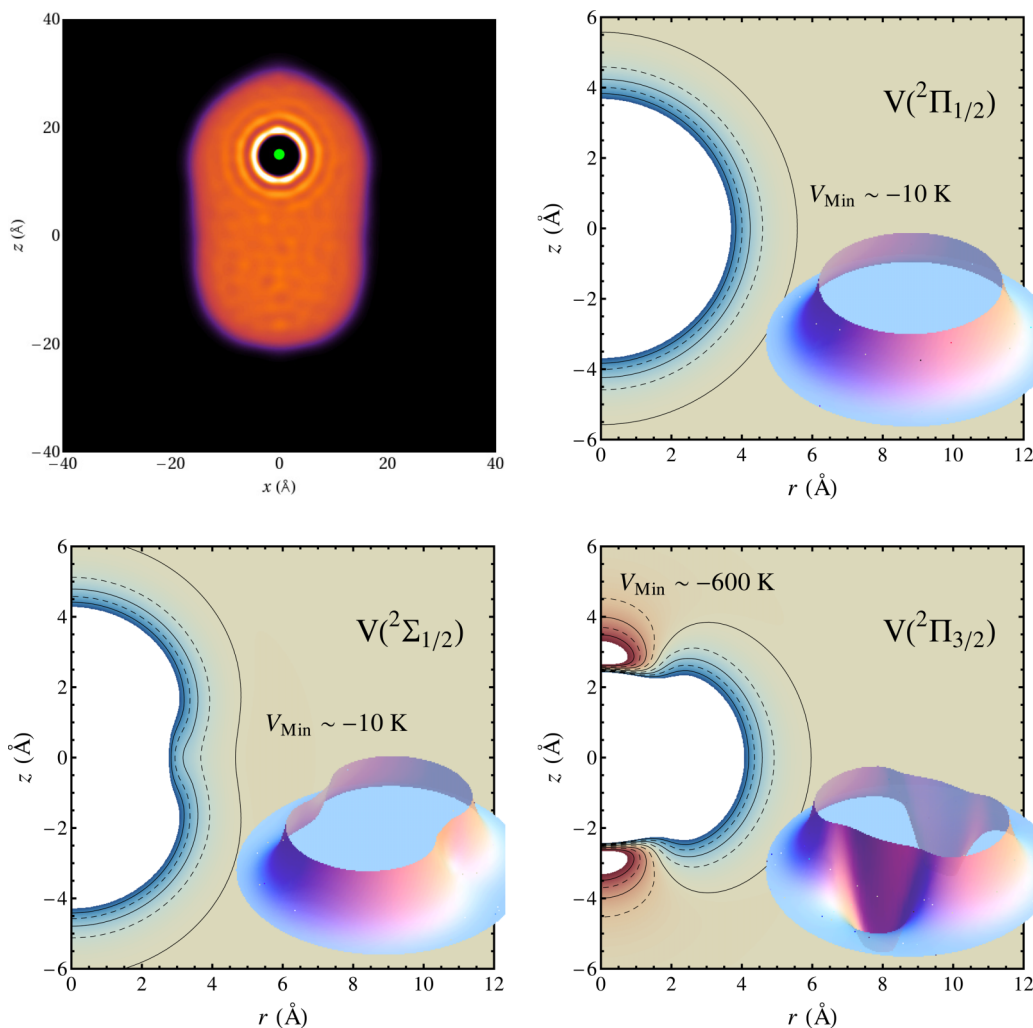
FIG. 6. Top left panel: Turning point of Ba$^+$ taken as starting configuration for the dynamics. The bright white spots correspond to high density regions. The other panels display the ^{2}P V_λ Ba$^+$–He potentials corresponding to this configuration. The isopotential lines are 100 K apart.

around the cation, the first term in the matrix defined by Eq. (8) is proportional to the identity.[61] As a result of the diagonalization one obtains the usual $J = 1/2$ and $J = 3/2$ eigenvectors pertaining to the spin-orbit interaction. However, when the cation is located off center, its environment is only axially symmetric. In this case, two of the V_{SO} eigenstates corresponding to $J = 3/2$ are eigenstates of the Hamiltonian $\mathcal{H}$, as are linear combinations of the other four. For the helium distributions considered here this effect turns out to be a small perturbation. The mixed eigenstates are such that they still have $\langle J \rangle \simeq 1/2$ and $\langle J \rangle \simeq 3/2$. This allows us to label the electronic states that we take as initial condition for the dynamics as $|\lambda\rangle = |3/2\rangle$ for the pure $J = 3/2$ state, and $|\lambda\rangle = |\widetilde{1/2}\rangle$ and $|\lambda\rangle = |\widetilde{3/2}\rangle$ for the mixed states. In a more conventional notation the $|\widetilde{1/2}\rangle$ configuration is referred to as ^{2}P$_{1/2}$ (D1), while the other two electronic states $|3/2\rangle$ and $|\widetilde{3/2}\rangle$ are referred to as the ^{2}P$_{3/2}$ (D2) configuration. There are different possibilities to label the excited states of the Ba$^+$-droplet complex. In the following we adhere to the Hund's case (a) notation, as discussed, e.g., in Ref. 65. In this scheme the electronic states are labeled as $^{2S+1}\Lambda_\Omega$, S being the spin of the system, Λ being the projection of the orbital angular momentum onto the axis, defined by the cation and

the COM of the helium droplet, and Ω being the projection of the total electronic angular momentum onto this axis.

The three V_λ potentials $V(^2\Pi_{1/2})$, $V(^2\Pi_{3/2})$, and $V(^2\Sigma_{1/2})$ corresponding to the eigenvectors $|\widetilde{1/2}\rangle$, $|3/2\rangle$, and $|\widetilde{3/2}\rangle$ respectively, are shown in Fig. 6 for the ρ_0 density corresponding to the selected turning point. Because the Σ pair potential is mostly repulsive and the Π pair potential has a deep attractive well, the resulting V_λ potentials, see Eq. (6), have quite different shapes. $V(^2\Pi_{1/2})$ is spherically symmetric and has a minimum of about 10 K at a distance of 6.5 Å and becomes repulsive at a distance of 5.5 Å. $V(^2\Sigma_{1/2})$ is similar but is not spherically symmetric as it has an annular minimum of about 10 K. The $V(^2\Pi_{3/2})$ potential reveals two deep wells with depths of about 600 K that are localized along the symmetry axis of the system. Hence, exciplex formation for this excited Ba$^+$ state is very likely. Indeed, in cold helium gas efficient exciplex formation has been detected for Ba$^+$ excited to the ^{2}P$_{3/2}$ state.[66]

The excited state potentials, V_λ, play a crucial role in the dynamical evolution of the system, see Eqs. (7). Their characteristics allows one to infer the outcome of the dynamics without performing actual time-dependent calculations. The depths of the $V(^2\Pi_{1/2})$ and $V(^2\Sigma_{1/2})$ potentials are rather
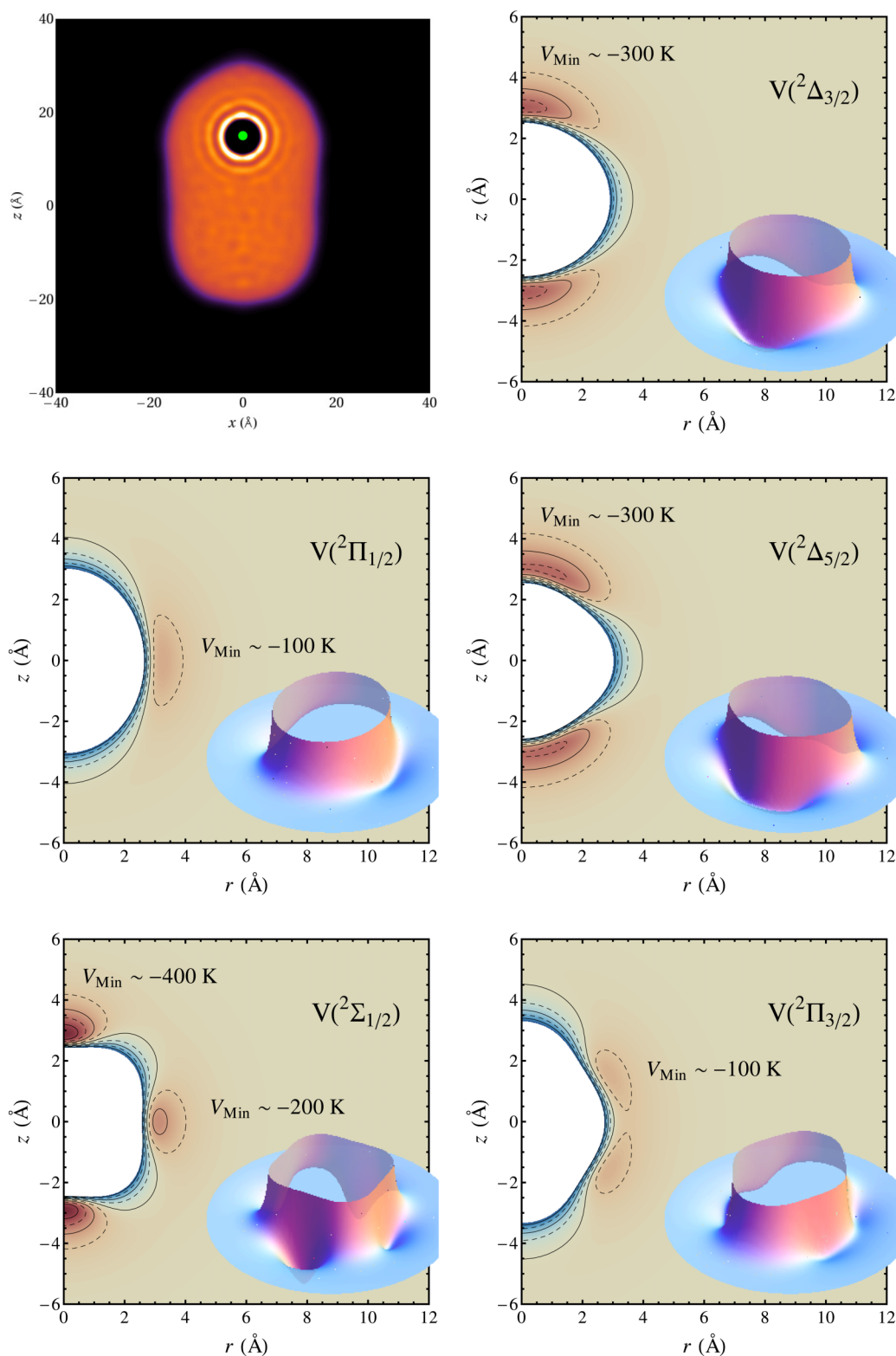
FIG. 7. ^{2}D V_λ Ba$^+$–He potentials corresponding to the same turning point configuration of Fig. 6 shown again in the top left panel. The isopotential lines are 100 K apart. The states $^2\Delta_{3/2}$ and $^2\Pi_{1/2}$ correlate with the ^{2}D$_{3/2}$ state, and the states $^2\Delta_{5/2}$, $^2\Sigma_{1/2}$, and $^2\Pi_{3/2}$ with the ^{2}D$_{5/2}$ state.

similar to that of the He-He potential. Consequently, it is questionable whether the Ba$^+$ cation will be ejected from the droplet if it is excited to any of the corresponding states. In contrast, the corresponding potentials for silver, which has been found to be ejected from the droplets, are much shallower.[36,39] Analogous to silver, the $V(^2\Pi_{3/2})$ potential is

very attractive and the excited Ba$^+$ is expected to remain attached to the droplet. To further assess the possible ejection, let us consider the Ancilotto parameter for these potentials[67] which is defined as $\lambda_A = \rho \epsilon r_{min}/(2^{1/6}\sigma)$, where ϵ and r_{min} are the depth and position of the He-impurity pair potential well, and ρ and σ are the density and surface tension of liquid

helium. For values of $\lambda_A \gtrsim 1.9$, the impurity will be solvated inside the liquid. The $V(^2\Pi_{1/2})$ and $V(^2\Sigma_{1/2})$ potentials yield $\lambda_A \sim 4.6$, suggesting that a Ba^+ cation excited to these states will not be ejected. For comparison, we find $\lambda_A \sim 0.5$ for Ag. Even if we consider the motion of the Ba^+ cation inside the droplet, ejection is very unlikely since the translational energy for a cation produced by photoexcitation of the neutral atom at the surface has been found to be small.[34] Finally, we would like to point out that the experimentally observed speed distributions of Ba^+ and Ag are quite different. While those of Ag are well described by a Gaussian with a cut off at high speeds, those of Ba^+ can be described by Maxwell-Boltzmann distribution. This seems to suggest that desolvation of both species is governed by different processes.

Having in mind these expectations, we have followed the dynamic evolution of the system for some particular starting configurations after photoexciting the Ba^+ cation. These correspond to turning points and passages through the droplet center as found in the dynamical calculations of the ground state Ba^+ ion; if the starting configuration is not a turning point, the initial velocity of the photoexcited cation, $\dot{\mathbf{r}}_{Ba_0^+}$, is that of the Ba^+ cation at the photoexcitation point. In the case corresponding to the turning point at 223 ps discussed above, we have found that after excitation of the Ba^+ cation to the $|^2\Sigma_{1/2}\rangle$ state, which is most favorable for ejection, the ion bubble first expands to adjust to the larger radius of the excited state, and eventually moves towards the center of the droplet. Similar observations have been made for other starting configurations. In all cases no ejection of the excited Ba^+ was found.

Additional calculations have been performed using as starting configuration the metastable stretched configuration corresponding to $\mathcal{Z}_0 = 44.6$ Å. Since the bubble containing the ion is larger in the excited states, excitation of the ion will cause an outgoing density wave which might lead to the breaking of the neck and lead to the desolvation of the Ba^+ cation. However, the calculations reveal that the density waves are unable to break the neck for this extreme configuration. This leads us to conclude that the excited Ba^+ cation is not ejected from the helium droplet within the present approach.

Analogous to the ^2P states, we have calculated the interaction potentials for the ^2D states of Ba^+. These states might play a role in the cation dynamics as they might become populated following radiative decay from the $^2P_{1/2}$ state of the cation. We present in the Appendix a generalization of the method of Ref. 36 to describe the dynamics in the ^2D manifold. Fig. 7 shows the Ba^+–He V_λ potentials relevant for the dynamics and the calculation of the emission spectrum presented in Sec. IV. These V_λ potentials are all very attractive with wells more than 100 K deep yielding cation bubbles whose radius is smaller than that of the ^2P states. Based on these characteristics of the potentials we conclude that it is unlikely that Ba^+ is ejected from the droplets after population of the ^2D states by radiative decay from ^2P states.

D. Exciplexes

Since the experiments reveal efficient Ba^+He_n exciplex formation, we have explored the formation of exciplexes

around Ba^+ $^2P_{1/2}$ and their possible ejection from the droplets. As we will show in Sec. IV, these exciplexes also play an important role in the emission spectrum of the photoexcited cation.

The rationale for this exploration is provided by diffusion Monte Carlo (DMC) calculations that found stable linear $Ba^+(^2\Pi_{1/2})He_2$ complexes with a distance of some 3 Å between the central Ba^+ ion and the two He atoms.[41] This distance is smaller than the radius of the excited cation bubble, as can be seen from Fig. 6. The bubble and linear configurations are separated by an energy barrier that apparently the TDDFT dynamics reported above has not been able to overcome. At variance, the formation of the $Ba^+(^2\Pi_{3/2})He_2$ complex is a barrierless process whose existence has been found in the present TDDFT dynamics. The DMC calculations furthermore reveal the existence of ring-like $Ba^+(^2\Pi_{1/2})He_n$ configurations for $n < 8$.[41]

Interestingly, linear and ring Cs^*He_n exciplexes were also found in solid helium[68–70] and discussed within a model that can be straightforwardly applied to Ba^+. Although being far much simpler than DFT and DMC approaches, the model is realistic enough to allow for a semi-quantitative description of $Ba^+(^2\Pi_{1/2})He_n$ and $Ba^+(^2\Pi_{3/2})He_n$ complexes. Thus, it is worth digressing from DFT and present its the results which will serve as a guide for more involved developments.

Following Refs. 68 and 71, the interaction between the Ba^+ cation and n He atoms is described by Eq. (8), fixing the origin of coordinates at the cation location and replacing the integral over the density by a sum on the He atoms. For the linear $n = 2$ configuration, both He atoms are axially located on opposite sides of the Ba^+ cation at a distance r. For the $n > 2$ ring configurations the He atoms are evenly distributed along a ring of radius r centered at the cation. The total He-He energy is then added to the cation-He interaction as a sum of pair interactions. We have taken for the He-He interaction the screened Lennard-Jones potential that enters the definition of the Orsay-Trento functional and have checked that the results presented below are sensibly the same if one uses the He-He Aziz potential.[72] After adding the spin-orbit interaction, one obtains the total energy of the complex as a function of r.

Diagonalizing the total energy for a given n as a function of r yields the PECs that correlate with the $^2P_{3/2}$ and $^2P_{1/2}$ He-cation potentials at long distances. Fig. 8 displays these PECs for $n = 2$ and 7. Both PEC reveal a minimum at $r \sim 3$ Å, indicating that linear and ring exciplexes can be formed for Ba^+ $^2\Pi_{1/2}$. The exciplex energy, taken as the well depth of the $Ba^+(^2\Pi_{1/2})He_n$ PEC, is displayed in Fig. 9 as a function of n. As for Cs^*He_n and Rb^*He_n exciplexes,[68,71] the exciplex energy increases with increasing n, except between $n = 2$ and $n = 3$. Eventually, for $n > 7$ the distance between neighboring He atoms becomes so small that the He-He repulsion starts to compete with the cation-He attraction. Also shown in this figure is the height of the energy barrier connecting the potential well and the free ion. It shows a dramatic increase going from $n = 2$ to $n = 3$, indicating that the formation of small exciplexes will be most efficient.

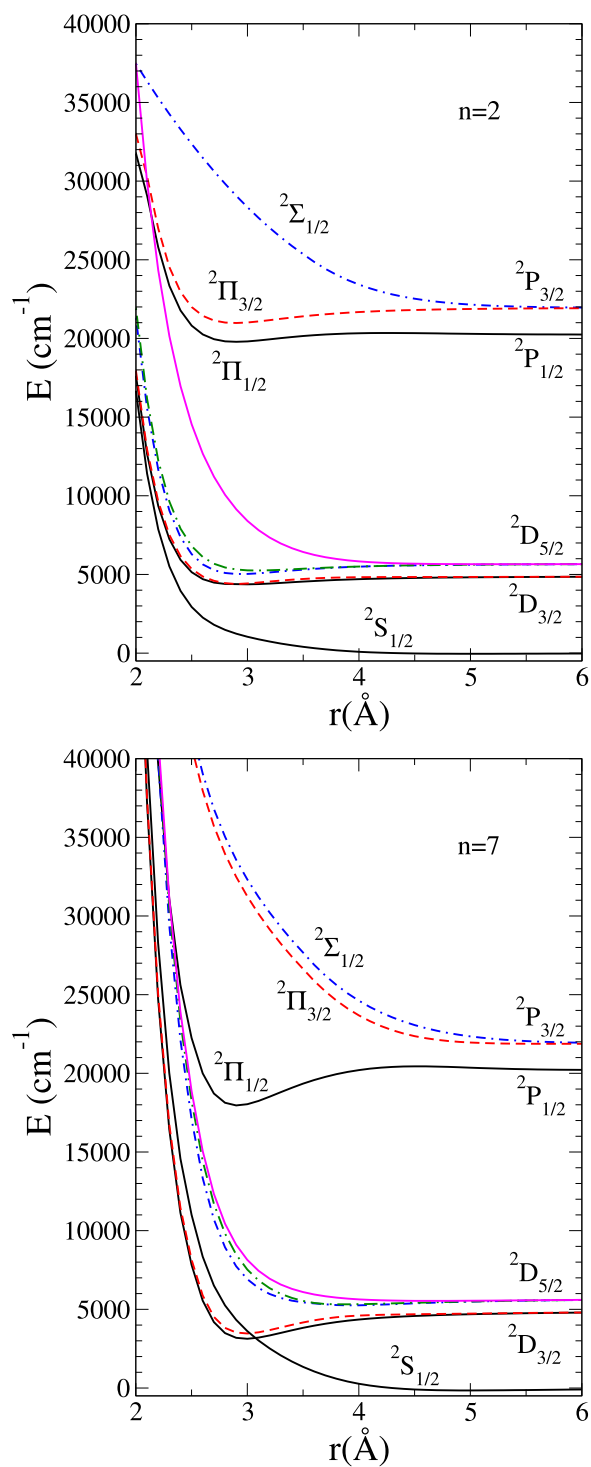The ^2D states can also be incorporated in the simplified exciplex model discussed above by using the expressions in
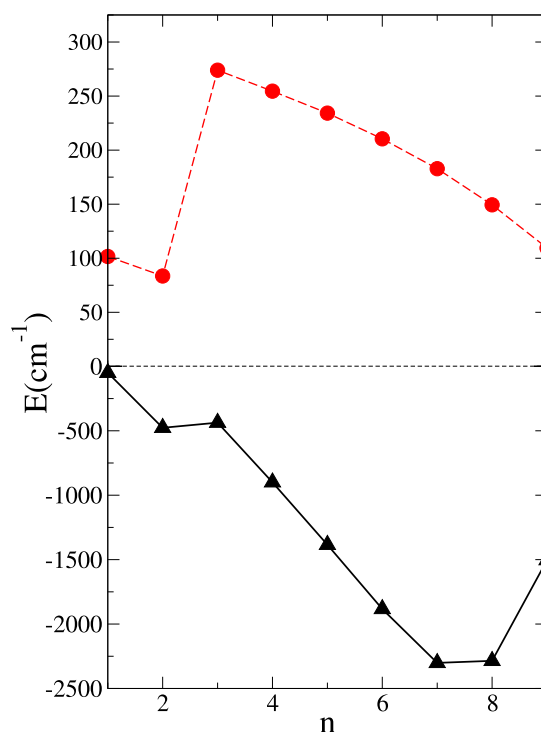
FIG. 9. Exciplex energy (bottom panel) and barrier height (top panel) of $Ba^+(^2\Pi_{1/2})He_n$ configurations as a function of n referred to the energy of the $^2P_{1/2}$ state of the Ba^+ cation.

IV. EMISSION SPECTRUM

As discussed above, $Ba^+(^2\Pi_{1/2})He_n$ exciplex formation might play a role in the dynamics and therefore has been addressed within the DFT approach. Before attempting to model the desolvation we first analyze the emission spectrum of the cation from the ^2P to the ^2S ground and the ^2D excited states. This allows us to verify the method by comparing the calculated emission spectra with those recorded in bulk helium.[10] The experimental emission spectrum was found to be identical for D1 and D2 excitations and to consist of three bands located at 491 nm (20 366 cm^{-1}), 523 nm (19 120 cm^{-1}), and 648 nm (15 432 cm^{-1}). A comparison of the free cation transitions and the experimental spectra indicates that the resonances at 20 366 cm^{-1} and 15 432 cm^{-1} likely correspond to the $^2S_{1/2} \leftarrow {}^2P_{1/2}$ and $^2D_{3/2} \leftarrow {}^2P_{1/2}$ transitions involving the $Ba^+(^2\Pi_{1/2})$ *bubble* configuration.[10,11] No emission lines were experimentally detected that could be associated to transitions from the $^2P_{3/2}$ state. This was interpreted that following excitation via the D2 band the population of the $^2P_{3/2}$ states quickly relaxes to the $^2P_{1/2}$ state.[10] Recently it has been argued[41] that the line observed at 19 120 cm^{-1}, for which no conclusive explanation was offered at the time, might arise from the emission from the $Ba^+(^2\Pi_{1/2})He_2$ exciplex.

To calculate the emission spectrum within DFT, we have to determine the relaxed helium configuration around the $|\lambda\rangle$ ^2P states—defined in Eq. (3)—of a Ba^+ cation located at the center of a $^4He_{1000}$ droplet. The size of this droplet is large enough to allow for a sensible comparison with the emission spectrum in bulk liquid helium. We look for stationary solutions to Eqs. (7) by introducing the usual t-dependence for stationary states

FIG. 8. Top panel: $Ba^+(^2\Pi_{1/2})He_2$ PEC as a function of the distance r between each He atom and the Ba^+ cation. Bottom panel: $Ba^+(^2\Pi_{1/2})He_7$ PEC as a function of the radius r of the ring exciplex. In both cases, for a given r we also display the energy of the ^2S and ^2D PEC obtained for the same linear or ring configuration.

the Appendix. A straightforward calculation similar to that carried out for the ^2P states yields the PECs in Fig. 8 that correlate to the $^2D_{5/2}$ and $^2D_{3/2}$ states of Ba^+ at large r values. For completeness and further reference we also show in the figure the He-Ba^+ PEC correlating to the $^2S_{1/2}$ state of the Ba^+ cation obtained by using the He-Ba^+ ground state pair potential.

$$\Psi_{He}(\mathbf{r},t) \rightarrow e^{-\iota \mu t/\hbar}\Psi_{He}(\mathbf{r}),$$
$$|\lambda(\mathbf{r},t)\rangle \rightarrow e^{-\iota \epsilon_\lambda t/\hbar}|\lambda(\mathbf{r})\rangle, \qquad (9)$$

where μ is the helium chemical potential and ϵ_λ is the eigenvalue of the electronic state of the excited Ba^+ in the presence of helium. Placing the impurity at $\mathbf{r}_{Ba^+} = 0$ and keeping it at rest, the relaxed configuration is obtained by solving the coupled equations

$$\left[-\frac{\hbar^2}{2m_{He}}\nabla^2 + \frac{\delta \mathcal{E}_{He}}{\delta \rho(\mathbf{r})} + V_\lambda(\mathbf{r}) \right]\Psi_{He} = \mu\,\Psi_{He},$$
$$\mathcal{H}|\lambda\rangle = \epsilon_\lambda\,|\lambda\rangle, \qquad (10)$$

where $V_\lambda(\mathbf{r})$ has been defined in Eq. (5). The procedure to determine the relaxed configuration is as follows:

1. Define a sensible helium density configuration, e.g., corresponding to the ground state Ba^+ cation at the center of the droplet.
2. Determine the internal electronic states corresponding to that helium density by diagonalizing Eq. (8). This yields three two-fold degenerate states $|\lambda\rangle$. Choose one of them and build the potential $V_\lambda(\mathbf{r})$, Eq. (5).
3. Using $V_\lambda(\mathbf{r})$, carry out a relaxation step as indicated by the first Eq. (10) to determine the new $\rho(\mathbf{r})$ and $\mathcal{H}$. Iterate until μ and ϵ_λ converge.

For the calculation of the emission spectrum we focus on the $V(^2\Pi_{1/2})$ potential, since all experimentally observed emission originates form the $^2P_{1/2}$ state. Fig. 10 shows the relaxed $Ba^+(^2\Pi_{1/2})$ bubble state (top left configuration) using the helium density configuration corresponding to the ground state Ba^+ cation as initial guess. Comparison of the helium density profiles reveals an increase of the ion bubble radius with approximately 1.2 Å. Upon convergence, the total energy of the droplet-Ba^+ complex is given by

$$E[\Psi,\mathbf{r},\lambda] = \int d\mathbf{r}\, \frac{\hbar^2}{2m_{He}}|\nabla\Psi|^2 + \int d\mathbf{r}\, \mathcal{E}_{He}[\rho]$$
$$+ \langle\lambda|V_{SO}|\lambda\rangle + \int d\mathbf{r}\, \rho(\mathbf{r})\,V_\lambda(\mathbf{r}). \qquad (11)$$

Evaluation of this expression reveals that relaxation of the helium lowers the energy of the system by 575 cm^{-1}, see Fig. 10.

The method outlined above works well provided the electronic state Hamiltonian is dominated by the spin-orbit term, as it is for bubble configurations. At variance, for
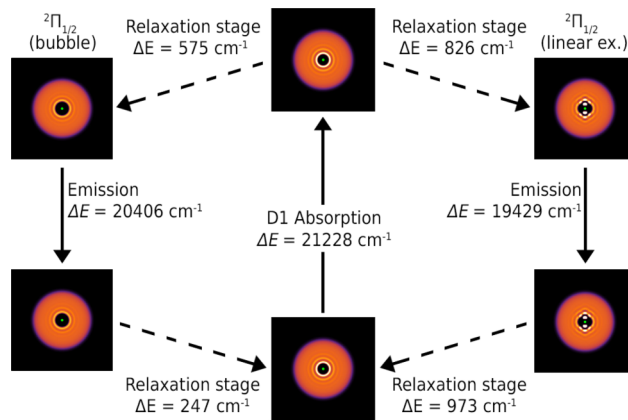

FIG. 10. Cation-helium configurations at different stages of the $^2S \rightarrow {}^2P \rightarrow {}^2S$ absorption-emission cycle. Left-hand cycle: Relaxation around the $Ba^+(^2\Pi_{1/2})$ bubble state. Right-hand cycle: Relaxation around the $Ba^+(^2\Pi_{1/2})$ linear exciplex. The energies of the radiative transitions and of the relaxation stages are indicated.

exciplex configurations the contribution of the helium term to Hamiltonian Eq. (8) has been found to be more sizeable and finding these configurations has required a somewhat different strategy, since the present method always leads to bubble configurations.

The $Ba^+(^2\Pi_{1/2})He_n$ exciplex configurations can be readily obtained by starting from a bubble configuration for the helium density supplemented with an electronic state $|\lambda\rangle$ appropriate for the sought-after exciplex. This state is previously determined within the simplified model of Refs. 68 and 71. Upon relaxation of both the helium density and electronic state, the exciplex configuration is obtained. Figure 11 shows two DFT configurations corresponding to a linear and ring exciplex similar to the DMC sampled configurations discussed in Ref. 41. It is worth noticing that the exciplexes persist as isolated entities even in the presence of the other helium atoms making up the droplet. More precisely, we find that both exciplexes are fully contained inside the cation bubble. Calculation of the energy reveals that the linear exciplex configuration is 251 cm^{-1} more stable than the relaxed bubble configuration, see Fig. 10. Based on the energetics one expects that excitation of the Ba^+ cation leads to exciplex formation, as experimentally observed.

Integrating the helium density inside the Ba^+ bubble we find that it corresponds to ^4He atoms for the linear structure,
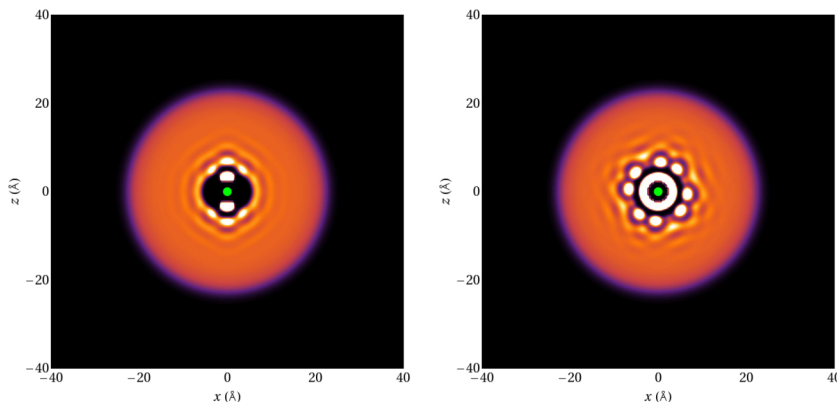

FIG. 11. Left panel: $Ba^+(^2P_{1/2})$ linear exciplex. Right panel: $Ba^+(^2P_{1/2})$ ring exciplex. Both exciplexes induce some replicas (density "blobs") at or near the cation bubble surface.
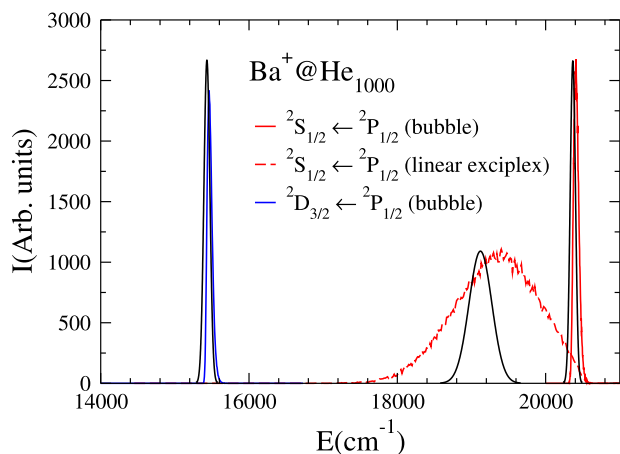
FIG. 12. Emission spectrum obtained from the de-excitation of the relaxed $^2P_{1/2}$ state of the Ba^+ cation. The gaussian lines in black are the experimental results of Ref. 10.

and to 12 atoms for the ring structure. The DFT approach thus has a tendency to overestimate the helium contents by about a factor of two in the regions of space where the fluid is strongly confined by very attractive interaction potentials. Hence, these high density spots should be taken with care if one identifies them with atoms. This drawback can only be cured by going beyond the fluid-like description inherent to DFT and switching to a discrete, atomic-like description, which is beyond the scope of the present work.

Once the relaxed helium configurations have been determined, their energies can be readily calculated. As can be seen in Fig. 10, for the ground state the exciplex is highest in energy. Based on these energy calculations the emission spectrum of the $Ba^+(^2\Pi_{1/2})$ linear exciplex is expected to be red-shifted with respect to that of the $Ba^+(^2\Pi_{1/2})$ bubble state by approximately 1000 cm^{-1}. The actual calculation of the emission spectrum proceeds in a way similar to that of the absorption spectrum as described, e.g., in Ref. 61. More relevant details of the procedure are given in the Appendix. Fig. 12 shows the calculated emission lines from the $Ba^+(^2\Pi_{1/2})$ bubble state to the $^2S_{1/2}$ and $^2D_{3/2}$ states, together with the emission line of the $Ba^+(^2\Pi_{1/2})$ linear exciplex state to the $^2S_{1/2}$ state. For comparison we also show the reconstructed experimental spectrum.[10] The agreement between theory and experiment is rather good, confirming the suggestion that the

experimentally observed line at 19 120 cm^{-1} corresponds to emission from the $Ba^+(^2\Pi_{1/2})$ linear exciplex to the ground state.[41] The larger linewidth found in the calculations for this transition is likely related to the overestimation of the number of helium atoms in the linear exciplex, as mentioned before. The transitions of the $Ba^+(^2\Pi_{1/2})$ linear exciplex to the various D states have also been calculated and fall in the region of 14 000–16 000 cm^{-1}. However, no experimental emission spectrum has been reported in this region of the spectrum.[10]

V. EXCIPLEX DYNAMICS

The experiments reveal a large yield of small Ba^+He_n exciplexes. In agreement with this result the static calculations find that the formation of linear exciplex is energetically favorable. To address the role of complexes in the dynamical evolution of the system we have investigated the complex formation within the TDDFT framework. As before, we arbitrarily start from the turning point configuration of ground state Ba^+ 223 ps after the ionization of the neutral Ba atom. But instead of taking as initial vector state $|\lambda\rangle$ an eigenstate of $\mathcal{H}$, we choose, as indicated in Sec. IV, a vector state corresponding to an exciplex configuration. The justification for this choice being that such a distribution will be probed by helium density fluctuations. As shown in the movies related to Fig. 13 (Multimedia view), we find that during the first picoseconds following the excitation the helium density adjusts to form a linear exciplex. This exciplex is tightly bound to the droplet and remains almost stationary while density waves travel through the helium droplet. Analogous to our observations for the bubble configurations discussed above we find that the exciplex is not ejected during the further evolution of the systems.

Inspection of the potential energy curves for the exciplexes in Fig. 8 reveals that at the exciplex $^2P_{1/2}$ equilibrium distance the energy of the ground state configuration is strongly increased. Consequently, upon radiative relaxation to the ground state this large amount of energy will be released into the droplet. To determine whether this could lead to the desolvation of Ba^+, we have followed the dynamics of the system after de-excitation. The results can be seen in the movies related to Fig. 13 (Multimedia view), where we show the formation of the linear exciplex when the cation is
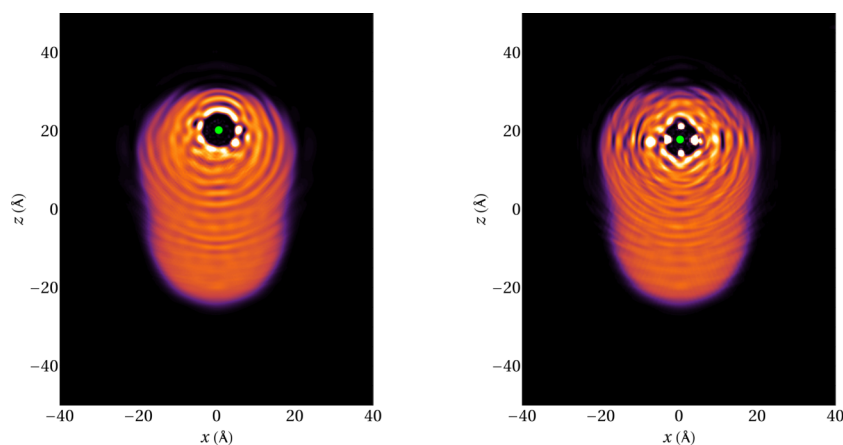

FIG. 13. 2D He densities 5 ps after de-excitation from the $P_{1/2}$ linear exciplex configuration to the $^2S_{1/2}$ (left) and $D_{3/2}$ states (right). (Multimedia view) [URL: http://dx.doi.org/10.1063/1.4942850.1][URL: http://dx.doi.org/10.1063/1.4942850.2]

about to reach the turning point at 223 ps and its subsequent evolution after being de-excited to the $^2S_{1/2}$ and $^2D_{3/2}$ states. To distinguish the formation and de-excitation stages, we have represented the cation with different colors, yellow for the former and green for the latter process. Inspection of the movies related to Fig. 13 (Multimedia view) reveals a fast formation of the exciplex as discussed above. After 5 ps the system is de-excited to either the $^2S_{1/2}$ or the $^2D_{3/2}$ state. In both cases, the helium quickly rearranges around the Ba^+ due to the change in interaction potential. As expected, relaxation to the $^2S_{1/2}$ ground state leads to the formation of a bubble configuration. In contrast, relaxation to the $^2D_{3/2}$ state leads to the formation of a non-linear exciplex. The transitional motion of the Ba^+ is found to depend strongly on the electronic state. After relaxation to the $^2D_{3/2}$ state the Ba^+ remains almost stationary, while following relaxation to the $^2S_{1/2}$ state the ion is accelerated towards the surface of the droplet. However, before the Ba^+ can escape from the droplet it is accelerated back towards the center of the droplet. Based on these results we conclude that radiative relaxation of Ba^+ $^2P_{1/2}$ does not lead to desolvation of the cation.

VI. DISCUSSION AND OUTLOOK

We have carried out a combined experimental and theoretical investigation of the dynamics of Ba^+ cations in helium droplets photoexcited to the 6p ^2P manifold. An analysis of the experimental results has been carried out within a full dynamical, three dimensional approach that combines a time-dependent DFT description of the helium with a classical dynamics description of the impurity. This theoretical approach has been successfully employed in the past to describe a wide variety of experimentally observed dynamical processes.[32–37] In the present study it successfully reproduces the experimental emission spectrum of the Ba^+ cation.[10] The calculated spectrum depends critically on the helium configurations around the excited $^2P\,Ba^+$ impurity. The good agreement with experiment implies that our DFT approach correctly describes the static and dynamic formation of Ba^+He_n exciplexes as well. In spite of these achievements, the method does not yield the desolvation of excited Ba^+ ions found in the experiments. This raises the question as to what causes this discrepancy.

A first issue to discuss in this context is the interpretation of the experimental data. The suggestion that Ba^+ cations are ejected from the helium droplets is based on time-of-flight mass spectra which reveal an increase in the number of Ba^+ ions and Ba^+He_n exciplexes accompanied by a reduction of signal corresponding to ion-containing helium droplets. However, the signal-to-noise ratio of the mass spectra on which this conclusion is based is rather low due to the presence of a large background in the mass range corresponding to the ion doped droplets. As a result it becomes difficult to determine whether the ion-doped droplet signal is depleted, which would indicate ejection of the ion, or shifted to lower mass which would be compatible with a (partial) evaporation of the droplet. Furthermore, it has not been possible to determine the state distribution of the Ba^+ cations, which could provide another indication on the desolvation process. However, the fact that

emission spectra of Ba^+ have been recorded in bulk helium indicates that non-radiative relaxation is not very efficient.[10] Although without additional information about the lifetime non-radiative relaxation cannot be completely ruled out, this result suggests that the excited Ba^+ cations are ejected from the droplets.

Experiments on Ag excited in helium droplets have revealed that the ejected atoms have a well-defined speed distribution, indicative of a critical Landau velocity.[19] In contrast, the speed distributions of the Ba^+ ions and Ba^+He_n exciplexes are best described by Maxwell-Boltzmann distributions. Such distributions suggest the presence of a thermally driven process, like evaporation. However, the temperatures corresponding to the observed speed distributions are found to be independent of droplet size and largest for excitation of the lowest energy state, $^2P_{1/2}$, see Fig. 3. This seems to contradict a simple thermally driven evaporative model. Hence, the experimental data are not conclusive regarding the desolvation mechanism of excited Ba^+ cations.

Concerning the theoretical description, one of the key ingredients is the interaction potentials between the Ba^+ cation and the helium. The potentials are calculated using the diatomics-in-molecule approach based on the Ba^+–He pair potentials. These have been computed at a high level of theory using large basis sets and have been corrected for basis set superposition errors. Comparison of the potentials with those using less accurate methods and smaller basis sets reveals only minor differences. We therefore expect that the potentials used are sufficiently accurate to correctly describe the dynamics of the excited system.

Since we use the diatomics-in-molecule approach for the interaction potentials, many-body interactions are not fully included. While neglecting such interactions is justified for weakly interacting neutral atoms, it is not obvious that this approach is justified for ionic species since the charge readily polarizes the surrounding helium. In order to estimate the effect of many-body interactions for the Ba^+–He_N system, we have explored three-body effects in the ground state of the Ba^+–He_2 complex. Computations have been performed at the CCSD(T) level of theory, adopting for barium and helium the same pseudopotential and basis set selected for the Ba^+–He ground state. No set of bond functions has been added, since test computations proved that their role in recovering three-body effects is negligible. The counterpoise correction has been performed using the scheme proposed by Valiron *et al.*[73] We have sampled the attractive and the repulsive regions of the PES in four sets of atomic arrangements: linear He–Ba^+–He and Ba^+–He–He, 90° bent He–Ba^+–He, and isosceles triangle with He-He as the basis. The general outcome of these computations is that three-body effects are very small (i.e., below 0.5 K) as far as the attractive part of the Ba^+–He_2 PES is considered, while they become significant at the repulsive region of the PES. However, this region is hardly sampled during the dynamical simulations.

Even though three-body effects are almost negligible with respect to the overall two-body contribution in the attractive region of the potential, theoretical computations performed on the Na^+–He_N[74] and Pb^+–He_N and Pb^{2+}–He_N[75] systems

indicate that they play a relevant role in the determination of the solvation structure of relatively small clusters. It was furthermore found that the charge-induced dipole interaction term in the cation-helium interaction pair potential tends to overestimate the binding energy of larger clusters. To address this effect we have repeated some simulations using diatomics-in-molecule potentials in which we have drastically decreased the value of this term in the *ab initio* Ba^+–He pair potentials. Even with this reduced attractive interaction we have found no evidence that the Ba^+ cation is ejected during the dynamics.

In addition to the potentials also the choice of the helium density functional plays an important role. The functional used in the present calculations has been constructed to be able to handle structured helium configurations such as those surrounding fairly attractive impurities like cations. The calculations yield very structured helium configurations corresponding to exciplexes, although the density is somewhat overestimated. Based on the good agreement between the calculated and experimentally observed absorption and emission spectra, however, we deem it unlikely that the choice of density functional is at the origin of the failure to reproduce the experimental results on the desolvation of excited Ba^+ ions.

In view of the above considerations regarding the accuracy of the calculations, it appears highly unlikely that excitation of a Ba^+ cations leads to its direct ejection from the helium droplet, either as bare ion or as a Ba^+He_n exciplex. The possibility that the cations are ejected from the droplets following radiative relaxation to the ^2D or ground state can be ruled out by the same arguments. This leaves non-radiative relaxation of the excited cations to the ^2D or the ^2S ground state as a possible explanation for the desolvation of the ions. Inspection of the Ba^+–He pair potentials and the Ba^+He_n exciplex potentials, Figs. 4 and 8, respectively, reveals that these states do not cross the ^2P states at energies accessible in the experiment. One therefore does not expect non-radiative relaxation to be an efficient process. Based on the same arguments one does not expect the relaxation from the $^2P_{3/2}$ to the $^2P_{1/2}$ state to be an efficient process. However, the emission spectra recorded for Ba^+ in bulk helium provide conclusive evidence that excitation of the $^2P_{3/2}$ is followed by a fast relaxation to the $^2P_{1/2}$ state. This could signify that non-adiabatic transitions which are not accounted for within the current theoretical model play a more important role than anticipated in the relaxation of excited atoms in helium droplets. Whether such transitions are important in the desolvation dynamics of excited Ba^+ cannot be answered for now and are worth a separate study.

To conclude, the present study indicates that elucidating the desolvation mechanism of excited Ba^+ ions will require additional experimental data, for example, on the state distribution of the desolvated Ba^+ cations, and an improved theoretical framework that, for example, includes non-adiabatic transitions between electronic states.[76]

APPENDIX: EXCITATION OF THE ^2D MANIFOLD

In this appendix we generalize the expressions of Subsection III C when the cation is excited to the ^2D manifold and give the essential details how the absorption spectrum has been calculated. To take advantage of the fast-Fourier techniques, we work in Cartesian coordinates. Our method is equivalent to that of Ref. 46 in which the PESs are expressed as a function of the spherical coordinates angles.

1. Pairwise sum approximation

The pair-interaction between an atom in a *s*-state and an atom in a *d*-state can be expressed in the basis $(|d_{xy}\rangle, |d_{yz}\rangle, |d_{z^2}\rangle, |d_{zx}\rangle, |d_{x^2-y^2}\rangle)$ as

$$
U(r) = \begin{pmatrix} V_\Delta(r) & 0 & 0 & 0 & 0 \\ 0 & V_\Pi(r) & 0 & 0 & 0 \\ 0 & 0 & V_\Sigma(r) & 0 & 0 \\ 0 & 0 & 0 & V_\Pi(r) & 0 \\ 0 & 0 & 0 & 0 & V_\Delta(r) \end{pmatrix}
$$

$$
\equiv V_\Delta(r)\{|d_{x^2-y^2}\rangle\langle d_{x^2-y^2}| + |d_{xy}\rangle\langle d_{xy}|\}
$$
$$
+ V_\Pi(r)\{|d_{yz}\rangle\langle d_{yz}| + |d_{zx}\rangle\langle d_{zx}|\} + V_\Sigma(r)|d_{z^2}\rangle\langle d_{z^2}|
$$
$$
= V_\Delta(r)\mathbf{I} + \{V_\Pi(r) - V_\Delta(r)\}\{|d_{yz}\rangle\langle d_{yz}| + |d_{zx}\rangle\langle d_{zx}|\}
$$
$$
+ \{V_\Sigma - V_\Delta(r)\}|d_{z^2}\rangle\langle d_{z^2}|, \tag{A1}
$$

where $V_\Delta(r)$, $V_\Pi(r)$, and $V_\Sigma(r)$ are the Ba^+–He pair potentials[41] and r is the distance between the cation and the He atom. For a system of N helium atoms, the total potential is approximated by the pairwise sum

$$
U = \sum_{n=1}^{N} \{V_\Delta(r_n)\mathbf{I} + [V_\Pi(r_n) - V_\Delta(r_n)]\, M_\Pi
$$
$$
+ [V_\Sigma(r_n) - V_\Delta(r_n)]\, M_\Sigma\}, \tag{A2}
$$

where r_n is the distance between the nth helium atom and the impurity and

$$
M_\Sigma = \mathcal{R}_n |d_{z^2}\rangle\langle d_{z^2}|\mathcal{R}_n^{-1},
$$
$$
M_\Pi = \mathcal{R}_n\{|d_{yz}\rangle\langle d_{yz}| + |d_{zx}\rangle\langle d_{zx}|\}\mathcal{R}_n^{-1}, \tag{A3}
$$

being $\mathcal{R}_n$ the rotation matrix that transform the unity vector $\hat{\mathbf{z}}$ into $\hat{\mathbf{r}}_n$, i.e., the unity vector in the cation-nth He atom direction. The matrices M_Σ and M_Π are symmetric. We define

$$d_0 \equiv (x^2 + y^2 + z^2)/r^2 = 1,$$
$$d_1 \equiv d_{xy} = \sqrt{3}\, xy/r^2,$$
$$d_2 \equiv d_{yz} = \sqrt{3}\, yz/r^2,$$
$$d_3 \equiv d_{z^2} = \frac{1}{2}\left(3z^2 - r^2\right)/r^2, \tag{A4}$$
$$d_4 \equiv d_{zx} = \sqrt{3}\, zx/r^2,$$
$$d_5 \equiv d_{x^2-y^2} = \frac{1}{2}\sqrt{3}\left(x^2 - y^2\right)/r^2,$$

where to simplify the notation, (x, y, z) are the components of the $\hat{\mathbf{r}}_n$ vector that connects the impurity with the given nth He atom. In terms of the $d's$, the elements of the matrices above can be written as follows:

$$M_\Sigma^{i,j} = d_i d_j,$$
$$M_\Pi^{1,1} = \frac{1}{3}\left(4d_5^2 + d_4^2 + d_2^2\right),$$
$$M_\Pi^{1,2} = -\frac{4}{3}d_1 d_2 + \frac{1}{\sqrt{3}}d_4 d_0,$$
$$M_\Pi^{1,3} = -\frac{2}{\sqrt{3}}d_2 d_4,$$
$$M_\Pi^{1,4} = -\frac{4}{3}d_1 d_4 + \frac{1}{\sqrt{3}}d_2 d_0,$$
$$M_\Pi^{1,5} = -\frac{4}{3}d_1 d_5,$$
$$M_\Pi^{2,2} = \frac{1}{3}\left(d_1^2 + d_4^2\right) + \left(d_3 + \frac{1}{\sqrt{3}}d_5\right)^2,$$
$$M_\Pi^{2,3} = \frac{1}{\sqrt{3}}d_1 d_4 - d_2\left(d_3 + \frac{1}{\sqrt{3}}d_5\right),$$
$$M_\Pi^{2,4} = -\frac{4}{3}d_2 d_4 + \frac{1}{\sqrt{3}}d_1 d_0, \tag{A5}$$
$$M_\Pi^{2,5} = -d_1 d_4 - \frac{1}{\sqrt{3}}d_2\left(d_3 + \frac{1}{\sqrt{3}}d_5\right),$$
$$M_\Pi^{3,3} = d_4^2 + d_2^2,$$
$$M_\Pi^{3,4} = \frac{1}{\sqrt{3}}d_1 d_2 - d_4\left(d_3 - \frac{1}{\sqrt{3}}d_5\right),$$
$$M_\Pi^{3,5} = \frac{1}{\sqrt{3}}\left(-d_4^2 + d_2^2\right),$$
$$M_\Pi^{4,4} = \frac{1}{3}\left(d_1^2 + d_2^2\right) + \left(d_3 - \frac{1}{\sqrt{3}}d_5\right)^2,$$
$$M_\Pi^{4,5} = d_1 d_2 + \frac{1}{\sqrt{3}}d_4\left(d_3 - \frac{1}{\sqrt{3}}d_5\right),$$
$$M_\Pi^{5,5} = \frac{1}{3}\left(4d_1^2 + d_4^2 + d_2^2\right).$$

The pairwise sum for U is transformed into a DFT expression by the substitution $\sum_n \rightarrow \int d\mathbf{r}' \rho(\mathbf{r}')$.[61]

2. Spin-orbit coupling

The SO interaction is semiempirically included assuming that the spin-orbit coupling is independent of the He-Ba$^+$ distance;[77] its strength is fixed to reproduce the spin-orbit splitting of bare Ba$^+$ in the 5d ^{2}D states, namely, 800.96 cm^{-1}.[62]

For the sake of completeness and future reference, we give the SO interaction in the basis used here, i.e.,

$|d_{xy}, 1/2\rangle, |d_{xy}, -1/2\rangle, |d_{yz}, 1/2\rangle, |d_{yz}, -1/2\rangle, |d_{z^2}, 1/2\rangle, |d_{z^2}, -1/2\rangle,$
$|d_{xz}, 1/2\rangle, |d_{xz}, -1/2\rangle, |d_{x^2-y^2}, 1/2\rangle, |d_{x^2-y^2}, -1/2\rangle,$ where the spin component $s = \uparrow (m_s = 1/2)$, $\downarrow (m_s = -1/2)$ is explicitly noted. We have $V_{SO} = \frac{1}{2} A_{\ell s} M_{SO}$ with $A_{\ell s}$ being 2/5 of the mentioned SO splitting and M_{SO} is the 10×10 matrix

$$
\begin{pmatrix}
0 & 0 & 0 & 1 & 0 & 0 & 0 & -i & 2i & 0 \\
0 & 0 & -1 & 0 & 0 & 0 & -i & 0 & 0 & -2i \\
0 & -1 & 0 & 0 & 0 & -i\sqrt{3} & i & 0 & 0 & -i \\
1 & 0 & 0 & 0 & -i\sqrt{3} & 0 & 0 & -i & -i & 0 \\
0 & 0 & 0 & i\sqrt{3} & 0 & 0 & 0 & -\sqrt{3} & 0 & 0 \\
0 & 0 & i\sqrt{3} & 0 & 0 & 0 & \sqrt{3} & 0 & 0 & 0 \\
0 & i & -i & 0 & 0 & \sqrt{3} & 0 & 0 & 0 & -1 \\
i & 0 & 0 & i & -\sqrt{3} & 0 & 0 & 0 & 1 & 0 \\
-2i & 0 & 0 & i & 0 & 0 & 0 & 1 & 0 & 0 \\
0 & 2i & i & 0 & 0 & 0 & -1 & 0 & 0 & 0
\end{pmatrix}.
$$

The electronic state Hamiltonian Eq. (8) is written as $\mathcal{H} = U + V_{SO}$ (the interaction U, Eq. (A1), is diagonal in spin and transformed into a 10×10 matrix to carry out the sum). As for ^{2}P states, diagonalization of $\mathcal{H}$ yields the five independent $V_\lambda(\mathbf{r})$ potentials for the ^{2}D manifold, each of them two-fold degenerate due to Kramer's theorem.[78,79] In the basis indicated above, the expression for the elements of the 10×10 matrix $\mathcal{V}(r)$ is

$$\mathcal{V}^{ijss'}(\mathbf{r}) = \Big\{ V_\Delta(\mathbf{r})\delta_{i,j} + [V_\Pi(\mathbf{r}) - V_\Delta(\mathbf{r})] M_\Pi^{ij}$$
$$+ [V_\Sigma(\mathbf{r}) - V_\Delta(\mathbf{r})] M_\Sigma^{ij} \Big\} \delta_{s,s'}. \tag{A6}$$

3. ^{2}P→^{2}S and ^{2}P→^{2}D radiative transitions

Since the cation is described classically and the electron orbitals are not explicitly considered, the emission spectrum is calculated by a semiclassical approximation of the vibrational Franck-Condon factors of an instantaneous transition from a given relaxed ^{2}P state.[61]

The emission to the ^{2}S state is obtained as the vertical transition of the cation from a relaxed state characterized by a helium density $\rho_\lambda^{2P}(\mathbf{r})$ associated with the V_λ^{2P} potential, namely,

$$\Delta\omega_{2S} = \int d\mathbf{r}\, \rho_\lambda^{2P}(\mathbf{r})\, [V_\lambda^{2P}(\mathbf{r}) - V_X(\mathbf{r})]. \tag{A7}$$

The emission to the ^{2}D states is similarly obtained

$$\Delta\omega_{2D} = \int d\mathbf{r}\, \rho_\lambda^{2P}(\mathbf{r})\, [V_\lambda^{2P}(\mathbf{r}) - V^{2D}(\mathbf{r})]. \tag{A8}$$

Expressions (A7) and (A8) give the atomic shift for the emission to the ^{2}S or ^{2}D state, i.e., the peak position for a given configuration $\rho_\lambda^{2P}(\mathbf{r})$ referenced to the emission energy of the free cation. The complete spectrum is obtained by the DF sampling method[80] that samples the DF density with the number of atoms in it, passing from a continuous to a discrete calculation of the transitions bearing a large similarity with the sampling method used within quantum Monte Carlo to obtain the spectrum,[78,81] there with walkers, here with "classical" atoms.

[1] R. L. Williams, Can. J. Phys. **35**, 134 (1957).

[2] D. R. Allum, P. V. E. McClintock, A. Phillips, and R. M. Bowley, Philos. Trans. R. Soc., A **284**, 179 (1977).

[3] V. Grau, M. Barranco, R. Mayol, and M. Pi, Phys. Rev. B **73**, 064502 (2006).

[4] H. J. Maris, J. Phys. Soc. Jpn. **77**, 111008 (2008).

[5] J. Poitrenaud and F. I. B. Williams, Phys. Rev. Lett. **32**, 1213 (1974).

[6] K. R. Atkins, Phys. Rev. **116**, 1339 (1959).

[7] B. Tabbert, H. Günther, and G. zu Putlitz, J. Low Temp. Phys. **109**, 653 (1997).

[8] M. W. Cole and R. A. Bachman, Phys. Rev. B **15**, 1388 (1977).

[9] B. Tabbert, M. Beau, H. Günther, W. Haussler, C. Honninger, K. Meyer, B. Plagemann, and G. zu Putlitz, Z. Phys. B **97**, 425 (1995).

[10] H. J. Reyher, H. Bauer, C. Huber, R. Mayer, A. Schafer, and A. Winnacker, Phys. Lett. A **115**, 238 (1986).

[11] H. Bauer, M. Beau, B. Friedl, C. Marchand, K. Miltner, and H. J. Reyher, Phys. Lett. A **146**, 134 (1990).

[12] A. Scheidemann, J. P. Toennies, and J. A. Northby, Phys. Rev. Lett. **64**, 1899 (1990).

[13] J. P. Toennies and A. F. Vilesov, Angew. Chem., Int. Ed. **43**, 2622 (2004).

[14] M. Y. Choi, G. E. Douberly, T. M. Falconer, W. K. Lewis, C. M. Lindsay, J. M. Merritt, P. L. Stiles, and R. E. Miller, Int. Rev. Phys. Chem. **25**, 15 (2006).

[15] F. Stienkemeier and K. K. Lehmann, J. Phys. B: At., Mol. Opt. Phys. **39**, R127 (2006).

[16] M. Hartmann, R. E. Miller, J. P. Toennies, and A. Vilesov, Phys. Rev. Lett. **75**, 1566 (1995).

[17] M. Hartmann, F. Mielke, J. P. Toennies, A. F. Vilesov, and G. Benedek, Phys. Rev. Lett. **76**, 4560 (1996).

[18] S. Grebenev, J. P. Toennies, and A. F. Vilesov, Science **279**, 2083 (1998).

[19] N. B. Brauer, S. Smolarek, E. Loginov, D. Mateo, A. Hernando, M. Pi, M. Barranco, W. J. Buma, and M. Drabbels, Phys. Rev. Lett. **111**, 153002 (2013).

[20] P. Claas, S. O. Mende, and F. Stienkemeier, Rev. Sci. Instrum. **74**, 4071 (2003).

[21] F. Bierau, P. Kupser, G. Meijer, and G. von Helden, Phys. Rev. Lett. **105**, 133402 (2010).

[22] L. Chen, J. Zhang, W. M. Freund, and W. Kong, J. Chem. Phys. **143**, 044310 (2015).

[23] X. H. Zhang and M. Drabbels, J. Phys. Chem. Lett. **5**, 3100 (2014).

[24] S. Smolarek, N. B. Brauer, W. J. Buma, and M. Drabbels, J. Am. Chem. Soc. **132**, 14086 (2010).

[25] X. H. Zhang, N. B. Brauer, G. Berden, A. M. Rijs, and M. Drabbels, J. Chem. Phys. **136**, 044305 (2012).

[26] A. I. G. Florez, D. S. Ahn, S. Gewinner, W. Schollkopf, and G. von Helden, Phys. Chem. Chem. Phys. **17**, 21902 (2015).

[27] J. M. Merritt, G. E. Douberly, and R. E. Miller, J. Chem. Phys. **121**, 1309 (2004).

[28] N. B. Brauer, S. Smolarek, X. H. Zhang, W. J. Buma, and M. Drabbels, J. Phys. Chem. Lett. **2**, 1563 (2011).

[29] F. Filsinger, D. S. Ahn, G. Meijer, and G. von Helden, Phys. Chem. Chem. Phys. **14**, 13370 (2012).

[30] X. Zhang and M. Drabbels, J. Chem. Phys. **137**, 051102 (2012).

[31] M. Barranco, R. Guardiola, E. S. Hernández, R. Mayol, J. Navarro, and M. Pi, J. Low Temp. Phys. **142**, 1 (2006).

[32] A. Leal, D. Mateo, A. Hernando, M. Pi, and M. Barranco, Phys. Chem. Chem. Phys. **16**, 23206 (2014).

[33] A. Leal, D. Mateo, A. Hernando, M. Pi, M. Barranco, A. Ponti, F. Cargnoni, and M. Drabbels, Phys. Rev. B **90**, 224518 (2014).

[34] D. Mateo, A. Leal, A. Hernando, M. Barranco, M. Pi, F. Cargnoni, M. Mella, X. Zhang, and M. Drabbels, J. Chem. Phys. **140**, 131101 (2014).

[35] A. Hernando, M. Barranco, M. Pi, E. Loginov, M. Langlet, and M. Drabbels, Phys. Chem. Chem. Phys. **14**, 3996 (2012).

[36] D. Mateo, A. Hernando, M. Barranco, E. Loginov, M. Drabbels, and M. Pi, Phys. Chem. Chem. Phys. **15**, 18388 (2013).

[37] J. von Vangerow, A. Stieg, F. Stienkemeier, M. Mudrich, A. Leal, D. Mateo, A. Hernando, M. Barranco, and M. Pi, J. Phys. Chem. A **118**, 6604 (2014).

[38] A. Braun and M. Drabbels, J. Chem. Phys. **127**, 114303 (2007).

[39] E. Loginov and M. Drabbels, J. Phys. Chem. A **111**, 7504 (2007).

[40] M. Lewerenz, B. Schilling, and J. P. Toennies, Chem. Phys. Lett. **206**, 381 (1993).

[41] M. Mella and F. Cargnoni, J. Phys. Chem. A **118**, 6473 (2014).

[42] I. S. Lim, H. Stoll, and P. Schwerdtfeger, J. Chem. Phys. **124**, 034107 (2006).

[43] F. Weigend and A. Baldes, J. Chem. Phys. **133**, 174102 (2010).

[44] F. Cargnoni and M. Mella, J. Phys. Chem. A **115**, 7141 (2011).

[45] M. W. Schmidt, K. K. Baldridge, J. A. Boatz, S. T. Elbert, M. S. Gordon, J. H. Jensen, S. Koseki, N. Matsunaga, K. A. Nguyen, S. Su, T. L. Windus, M. Dupuis, and J. A. Montgomery, J. Comput. Chem. **14**, 1347 (1993).

[46] F. Cargnoni, A. Ponti, and M. Mella, Phys. Chem. Chem. Phys. **15**, 18410 (2013).

[47] F. Stienkemeier, F. Meier, and H. O. Lutz, Eur. Phys. J. D **9**, 313 (1999).

[48] E. Loginov and M. Drabbels, J. Chem. Phys. **136**, 154302 (2012).

[49] A. Hernando, R. Mayol, M. Pi, M. Barranco, F. Ancilotto, O. Bünermann, and F. Stienkemeier, J. Phys. Chem. A **111**, 7303 (2007).

[50] F. Ancilotto, E. Cheng, M. W. Cole, and F. Toigo, Z. Phys. D **98**, 323 (1995).

[51] C. C. Lovallo and M. Klobukowski, J. Chem. Phys. **120**, 246 (2004).

[52] F. Dalfovo, A. Lastri, L. Pricaupenko, S. Stringari, and J. Treiner, Phys. Rev. B **52**, 1193 (1995).

[53] F. Ancilotto, M. Barranco, F. Caupin, R. Mayol, and M. Pi, Phys. Rev. B **72**, 214522 (2005).

[54] M. Frigo and S. G. Johnson, Proc. IEEE **93**, 216 (2005).

[55] A. Hernando, M. Barranco, R. Mayol, M. Pi, and F. Ancilotto, Phys. Rev. B **78**, 184515 (2008).

[56] M. Guilleumas, F. Garcias, M. Barranco, M. Pi, and E. Suraud, Z. Phys. D **26**, 385 (1993).

[57] L. Giacomazzi, F. Toigo, and F. Ancilotto, Phys. Rev. B **67**, 104501 (2003).

[58] L. Lehtovaara, T. Kiljunen, and J. Eloranta, J. Comput. Phys. **194**, 78 (2004).

[59] M. Weissbluth, *Atoms and Molecules* (Academic Press, New York, 1980).

[60] F. O. Ellison, J. Am. Chem. Soc. **85**, 3540 (1963).

[61] A. Hernando, M. Barranco, R. Mayol, M. Pi, and M. Krośnicki, Phys. Rev. B **77**, 024513 (2008).

[62] A. Kramida, Y. Ralchenko, and J. Reader, NIST ASD Team, NIST Atomic Spectra Database, version 5.0, National Institute of Standards and Technology, Gaithersburg, MD, 2012, available at: http://physics.nist.gov/asd.

[63] A. Ralston and H. S. Wilf, *Mathematical Methods for Digital Computers* (John Wiley and Sons, New York, 1960).

[64] D. Mateo, D. Jin, M. Barranco, and M. Pi, J. Chem. Phys. **134**, 044507 (2011).

[65] A. Pifrader, O. Allard, G. Auböck, C. Callegari, W. E. Ernst, R. Hubert, and F. Ancilotto, J. Chem. Phys. **133**, 164502 (2010).

[66] Y. Fukuyama, Y. Mortiwaki, and Y. Matsuo, Phys. Rev. A **69**, 042505 (2004).

[67] F. Ancilotto, P. B. Lerner, and M. W. Cole, J. Low Temp. Phys. **101**, 1123 (1995).

[68] D. Nettels, A. Hofer, P. Moroshkin, R. Müller-Siebert, S. Ulzega, and A. Weis, Phys. Rev. Lett. **94**, 063001 (2005).

[69] M. Zbiri and C. Daul, Phys. Lett. A **341**, 170 (2005).

[70] P. Moroshkin, A. Hofer, and A. Weis, Phys. Rep. **469**, 1 (2008).

[71] A. Hofer, P. Moroshkin, D. Nettels, S. Ulzega, and A. Weis, Phys. Rev. A **74**, 032509 (2006).

[72] R. A. Aziz and A. R. Janzen, Phys. Rev. Lett. **74**, 1586 (1995).

[73] P. Valiron and I. Mayer, Chem. Phys. Lett. **275**, 46 (1997).

[74] N. Issaoui, K. Abdessalem, H. Ghalla, S. J. Yaghmour, F. Calvo, and B. Ouija, J. Chem. Phys. **141**, 174316 (2014).

[75] P. Slavíček and M. Lewerenz, Phys. Chem. Chem. Phys. **12**, 1152 (2010).

[76] E. Loginov, A. Hernando, J. A. Beswick, N. Halberstadt, and M. Drabbels, J. Phys. Chem. A **119**, 6033 (2015).

[77] J. L. Persson, Q. Hui, Z. J. Jakubek, M. Nakamura, and M. Takami, Phys. Rev. Lett. **76**, 1501 (1996).

[78] A. Nakayama and K. Yamashita, J. Chem. Phys. **114**, 780 (2001).

[79] P. H. E. Meier and E. Bauer, *Group Theory* (North-Holland, Amsterdam, 1962).

[80] D. Mateo, A. Hernando, M. Barranco, R. Mayol, and M. Pi, Phys. Rev. B **83**, 174505 (2011).

[81] J. Navarro, D. Mateo, M. Barranco, and A. Sarsa, J. Chem. Phys. **136**, 054301 (2012).